

Diverse polymorphism in Ruddlesden-Popper chalcogenides

Prakriti Kayastha,¹ Erik Fransson,² Paul Erhart,² and Lucy Whalley^{1,*}

¹*Department of Mathematics, Physics and Electrical Engineering,
Northumbria University, Newcastle upon Tyne, NE1 8QH, United Kingdom*

²*Department of Physics, Chalmers University of Technology, SE-41296, Gothenburg, Sweden
(Dated: July 16, 2025)*

Ruddlesden-Popper (RP) chalcogenides are stable, non-toxic candidates for optoelectronic or thermoelectric applications. The structural diversity of RP oxides is already exploited to tune properties or achieve more advanced functionalities like multiferroicity, however, little is known about the structural evolution of RP chalcogenides. In this work, we develop a high-accuracy machine-learned interatomic potential to run large-scale molecular dynamics simulations on $\text{Ba}_{n+1}\text{Zr}_n\text{S}_{3n+1}$ for $n = 1$ to $n = 6$. We predict new polymorphs for each n -value, calculate their corresponding phase transition temperatures, and validate our approach through comparison to published experimental results. We find that the $n = 1$ phase exhibits negative thermal expansion, that $n = 1$ and $n = 3$ undergo unusual ascending symmetry breaking, and that phases with $n \geq 4$ form layer-dependent tilt patterns previously unreported for inorganic RP materials. This unique behaviour results from competition between octahedral rotations and rumpling at the rocksalt interface, and suggests new strategies for accessing advanced functionalities.

Three-dimensional corner-sharing octahedra form the fundamental building blocks in perovskite materials. Quasi-two-dimensional perovskite analogues, formed from single or multiple layers of perovskite intercalated with thin sheets of inorganic or organic materials, are also widely reported. One example is the Ruddlesden-Popper (RP) series, $\text{A}_{n+1}\text{B}_n\text{X}_{3n+1}$, in which perovskite slabs are separated by rocksalt layers (Fig. 1a). The RP dimensionality (controlled through the n -value) provides a mechanism for tuning material properties such as band gap, ion mobility, and thermal conductivity [1–4].

Oxides are the most established class of RP materials, and are known to display a range of advanced functionality, including superconductivity, ferroelectricity, and negative thermal expansion [5–9], where crystal symmetry plays a crucial role in determining whether a material will exhibit these properties [10]. The symmetry can be engineered through access to various RP polymorphs, which are closely related through small structural distortions often involving octahedral tilts or cation displacements (Fig. 1b–e).

Perovskite and RP chalcogenides (with $\text{X}=\text{S},\text{Se}$) have emerged more recently as candidate materials for optoelectronic and thermoelectric applications [11–22]. BaZrS_3 , the most studied example, exhibits several promising properties, including strong visible light absorption, defect tolerance, and chemical stability [23–27]. The equivalent RP material, $\text{Ba}_{n+1}\text{Zr}_n\text{S}_{3n+1}$, has been synthesised with $n = 1$ to 3 [28–32]. At moderate temperatures Ba_2ZrS_4 ($n = 1$) and $\text{Ba}_3\text{Zr}_2\text{S}_7$ ($n = 2$) form in the highly symmetric $I4/mmm$ phase, with untilted octahedra along all three axes, as in the high-temperature $Pm\bar{3}m$ cubic phase of the 3D perovskite [33]. Distortions to lower symmetry phases are expected with decreasing temperature, as is observed for other perovskites and RP materials, but have not yet been investigated through

theory or experiment. Here, we explore how this new material family evolves with temperature and n -value, revealing a range of polymorphs with unexpected behaviours.

We started by considering the 33 tilted structures enumerated by Aleksandrov et al. [34]. With these we constructed a neuroevolution potential (NEP) to run

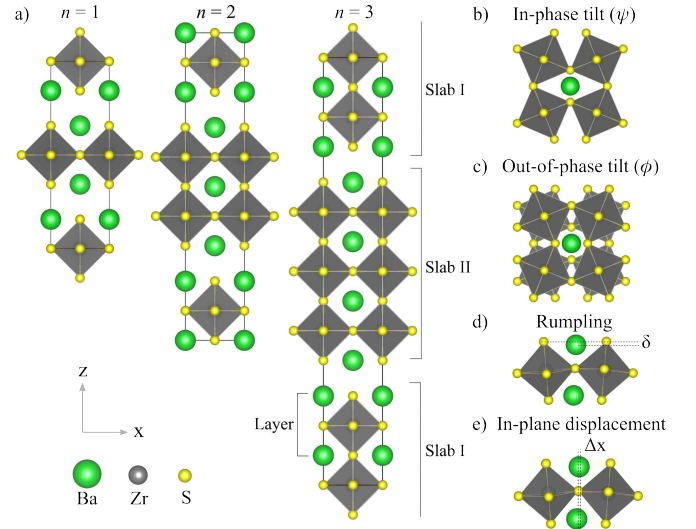


FIG. 1. a) $\text{A}_{n+1}\text{B}_n\text{X}_{3n+1}$ Ruddlesden-Popper crystal structures. The primitive cell is formed from two unique perovskite slabs with a half-cell offset. Each slab contains n layers of BX_6 octahedra, such that the $n = \infty$ limit is equivalent to ABX_3 . Here the A-site, B-site and X-site are Ba (green), Zr (grey) and S (yellow), respectively. Schematics of b) in-phase (ψ) and c) out-of-phase (ϕ) octahedral tilting; d) rumpling distortion; d) in-plane A-site displacement. The rumpling amplitude is defined as positive when A-site cations at the rock-salt layer move towards the BX_6 octahedra. In-plane refers to displacements along the x - or y -axes.

TABLE I. Predicted ground state tilt patterns and resulting space groups for $\text{Ba}_{n+1}\text{Zr}_n\text{S}_{3n+1}$ materials, where n is the number of perovskite layers within each slab. Aleksandrov notation is used to denote the out-of-phase (ϕ) and in-phase (ψ) octahedral tilts along each axis, with an overbar to indicate that the tilt patterns between adjacent slabs are in opposite directions [52].

n	Slab I	Slab II	Space group
1	$\phi 00$	$0\bar{\phi}0$	$P4_2/ncm$
2	$\phi 00$	$0\phi 0$	$P4_2/mnm$
3	$\phi 00$	$0\bar{\phi}0$	$P4_2/ncm$
4	$\phi\phi\psi$	$\phi\phi\bar{\psi}$	$Pnma$
5	$\phi\phi\psi$	$\phi\phi\psi$	$P2_1/c$
6	$\phi\phi\psi$	$\phi\phi\bar{\psi}$	$Pnma$

molecular dynamics (MD) simulations of the RP series $\text{Ba}_{n+1}\text{Zr}_n\text{S}_{3n+1}$ using the GPUMD package [35–37]. The NEP model, based on hybrid density functional theory (DFT) calculations [38–40], provides an accurate description of the anharmonic potential energy surface, and allows us to predict the temperature-dependent structural evolution across a wide range of n -values. Further computational details are provided in the Supplemental Material [41–51].

In Table I, we display the predicted ground-state tilt patterns of the RP materials with $n = 1$ to $n = 6$. We identify two categories. The first category comprises the low n -value RP phases, from $n = 1$ to $n = 3$, where slab I has a single out-of-phase tilt along the x -axis, and slab II has a single out-of-phase tilt along the y -axis (see Fig. 1). The second category consists of the high n -value RP phases with $n = 4, 5, 6$. Here there is increased tilting in both slabs, with out-of-phase tilts along the x - and y -axes, and an in-phase tilt along z . BaZrS_3 has the same tilt pattern in the low-temperature $Pnma$ structure, so we conclude that the $\text{Ba}_{n+1}\text{Zr}_n\text{S}_{3n+1}$ ground state structures converge to that of the parent perovskite for $n \geq 4$. For low- n RP materials, the octahedral tilting is hindered by the higher density of rocksalt layers. We note that for all n -values the ferroelectric $Cmc2_1$ phase is metastable, but very close in energy (0.04 meV to 2 meV) to the paraelectric ground states. NEP-calculated energies for all possible tilt patterns across $n = 1$ to 6 are given in the Supplemental Material [41].

To investigate how the RP structures evolve with temperature we perform MD heating runs starting from the ground-state polymorphs at 0 K. The in-plane lattice parameters (Fig. 2a) and heat capacities (Fig. 2b) reiterate our finding that there are two n -value categories. The low- n ($1 \leq n \leq 3$) lattice parameters are clustered around 5.06 Å and the high- n ($n \geq 4$) parameters are clustered around 5.01 Å. This grouping reflects the shared tilt patterns, as discussed above, with tilting along both in-plane axes for high- n driving contraction of the lattice parameter. For all high- n materials the

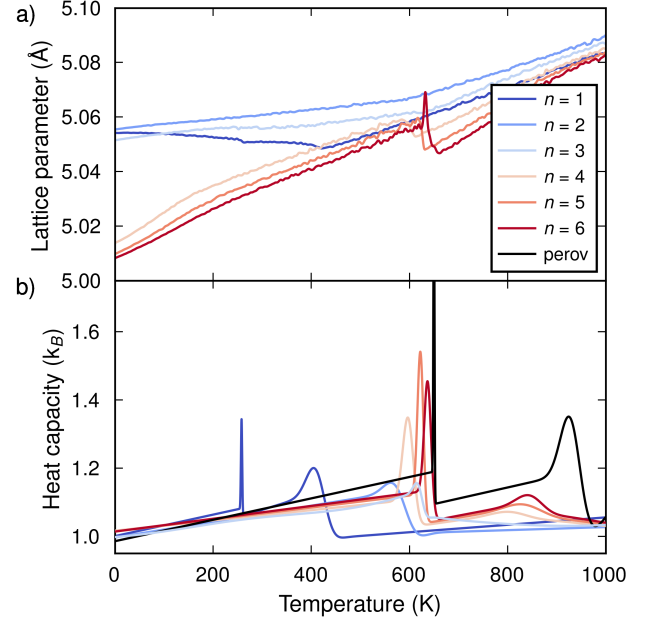


FIG. 2. Thermodynamic observables for $\text{Ba}_{n+1}\text{Zr}_n\text{S}_{3n+1}$: a) in-plane lattice parameters; b) heat capacities. A sharper peak in the heat capacity indicates a first-order (discontinuous) phase transition, whilst a broader peak indicates more second-order (continuous) character.

heat capacity shows the signature of two phase transitions: a low-temperature transition with first-order character, and a high-temperature transition with second-order character. As the n -value increases, there is a clear convergence towards the 3D perovskite phase transitions at 650 K and 900 K. The character of each phase transition is determined through the heat capacity peak width and projections onto the octahedral tilt phonon modes (available in the Supplemental Material).

The lattice parameters show that Ba_2ZrS_4 exhibits negative in-plane thermal expansion. Negative thermal expansion has been previously reported for RP oxides with $n = 1$, where it is associated with soft phonon modes and anisotropic elastic constants [9, 53]. The temperature range over which it occurs here—up to the second-order phase transition at 420 K—is larger than that reported for the RP oxides. Recent calculations at the quasi-harmonic level of theory predict negative thermal expansion in $\text{Ba}_3\text{Zr}_2\text{S}_7$ at very low temperature (< 10 K), which we do not reproduce here [54].

A summary of all predicted polymorphs and transition temperatures, for the RP materials with $n = 1$ to 6 and perovskite, is shown in Fig. 3. The polymorphs are identified through projections onto the octahedral tilt phonon modes which are reported, along with the corresponding tilt patterns in Aleksandrov notation, in the Supplemental Material [41]. For RP materials with $n = 1, 2, 3$ there are three distinct structural evolutions with temperature.

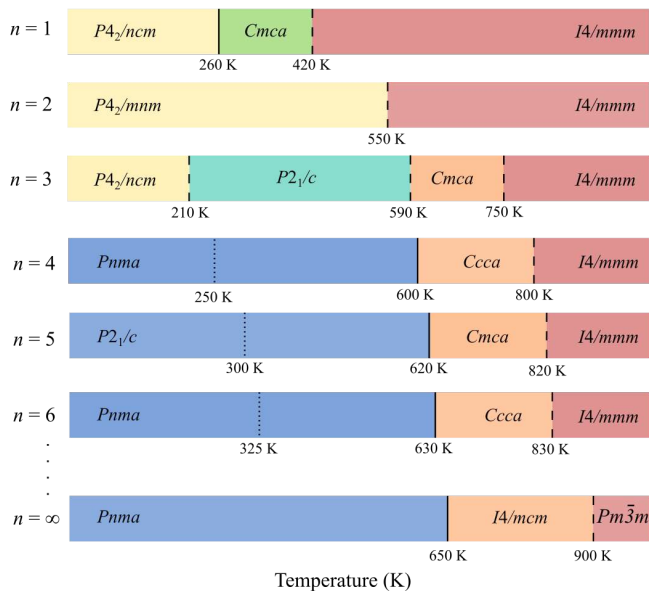


FIG. 3. A summary of the space groups, tilt patterns, and phase transition temperatures for $Ba_{n+1}Zr_nS_{3n+1}$ with $n = 1$ to 6 and $n = \infty$ (perovskite). The bars are colour-coded by tilt pattern (specified in the Supplemental Material [41]). The space group, indicated in text, is determined by both the tilt pattern and whether the n -value is odd or even. Solid, dashed, and dotted lines indicate first-order and second-order phase transitions as well as surface transitions, respectively.

In contrast, the sequence of tilt patterns for all RP phases with $n \geq 4$ are equivalent, and are equal to that of the parent perovskite. By 900 K all RP and perovskite materials have transitioned to the untilted $I4/mmm$ parent structure.

We calculate the X-ray diffraction (XRD) patterns for Ba_2ZrS_4 and $Ba_3Zr_2S_7$ to compare against the available experimental data (see figures in Supplemental Material [29, 41, 55]). For $Ba_3Zr_2S_7$ we find strong agreement between simulation and experiment, confirming that the $P4_2/mnm$ phase forms at 300 K, and validating our overall approach [55]. For Ba_2ZrS_4 two phase transitions occur near room temperature. The $Cmca$ to $I4/mmm$ transition is second-order, so the corresponding XRD peaks are expected to diminish gradually, making the phases more challenging to distinguish. We tentatively assign the space group as $Cmca$. Further XRD measurements on a single crystal sample, combined with complementary techniques such as Raman spectroscopy, could aid in a more definitive determination of the crystal structure.

Both the $P4_2/ncm$ to $Cmca$ transition in Ba_2ZrS_4 and the $P4_2/ncm$ to $P2_1/c$ transition in $Ba_4Zr_3S_{10}$ correspond to a reduction in symmetry with increasing temperature. Ascending symmetry breaking is highly unusual; generally the more symmetrical phase corresponds to higher temperatures [56]. Symmetry breaking with

increasing temperature usually suggests that there are several competing interactions near the phase-transition boundary with similar energy scales [57]. For Ba_2ZrS_4 the symmetry lowering results from a first-order transition to a system with increased in-plane octahedral tilting, and is concurrent with the in-plane negative thermal expansion, whereas notably in $Ba_4Zr_3S_{10}$ the symmetry lowering occurs via a continuous transition.

To understand the microscopic mechanism underlying this process in $Ba_4Zr_3S_{10}$ we analyse the layer-by-layer tilt angles of the ZrS_6 octahedra along each axis, and at four separate temperatures. For $Ba_4Zr_3S_{10}$ the tilt configuration is $\phi 00\ 0\phi 0$ ($P4_2/ncm$) at 1 K (Fig. 4a). At 300 K, the system has transitioned to a lower symmetry phase, $\phi 0\psi\ 0\bar{\phi}\psi$ ($P2_1/c$), with z -axis tilting in the middle layer of each slab only. Similar interface effects, where the tilt angle is dependent on the distance from the rocksalt interface, have been previously observed in simulations of hybrid halide RP materials [50]. This is, to our knowledge, the first report for inorganic RP materials.

We also examine the tilting in $Ba_5Zr_4S_{13}$ as an example of large- n behaviour. For $Ba_5Zr_4S_{13}$ the tilt configuration is $\phi\phi\psi\ \phi\phi\bar{\psi}$ ($Pnma$) at 1 K (Fig. 4b). At 300 K, z -axis tilting at the rocksalt interface is suppressed, but there is no change in space group. We refer to this as a surface transition.

Although $Ba_4Zr_3S_{10}$ and $Ba_5Zr_4S_{13}$ exhibit different transitions at lower temperatures, at higher temperatures they show the same structural evolution. At 650 K both materials have no in-plane tilting, but out-of-plane tilting in the interior layer(s) remains. At 1000 K both have transitioned to the untilted $I4/mmm$ parent structure. This mimics the phase transitions of perovskite, which undergoes the same sequence of tilt patterns, from $a^0a^0c^-$ (out-of-phase tilting along the z -axis only) to $a^0a^0a^0$ (no tilting along any axis).

The key difference between perovskite and RP materials is that the latter features interface effects at the rocksalt layer. We see this through the layer-dependent tilt patterns discussed above. It also manifests through the low-temperature structures predicted for $n = 1$ to $n = 3$, where the in-plane tilts are along perpendicular axes for neighbouring slabs (Fig. 4a). This is very distinct from the low-temperature tilt configuration for perovskite and high- n RP materials, where there is tilting along all axes and in both slabs. The distinction stems from the fact that low- n materials have a higher density of perovskite layers at the rocksalt interface, and so the effects from these interfaces are more pronounced.

To better understand the impact of the BaS rocksalt layer on phase transitions, we move beyond octahedral tilting and analyse the Ba displacements. Out-of-plane A-site displacement at the rocksalt layer is termed “rumpling” as the A and X ions no longer lie in the same plane [58]. We plot the rumpling amplitude as a func-

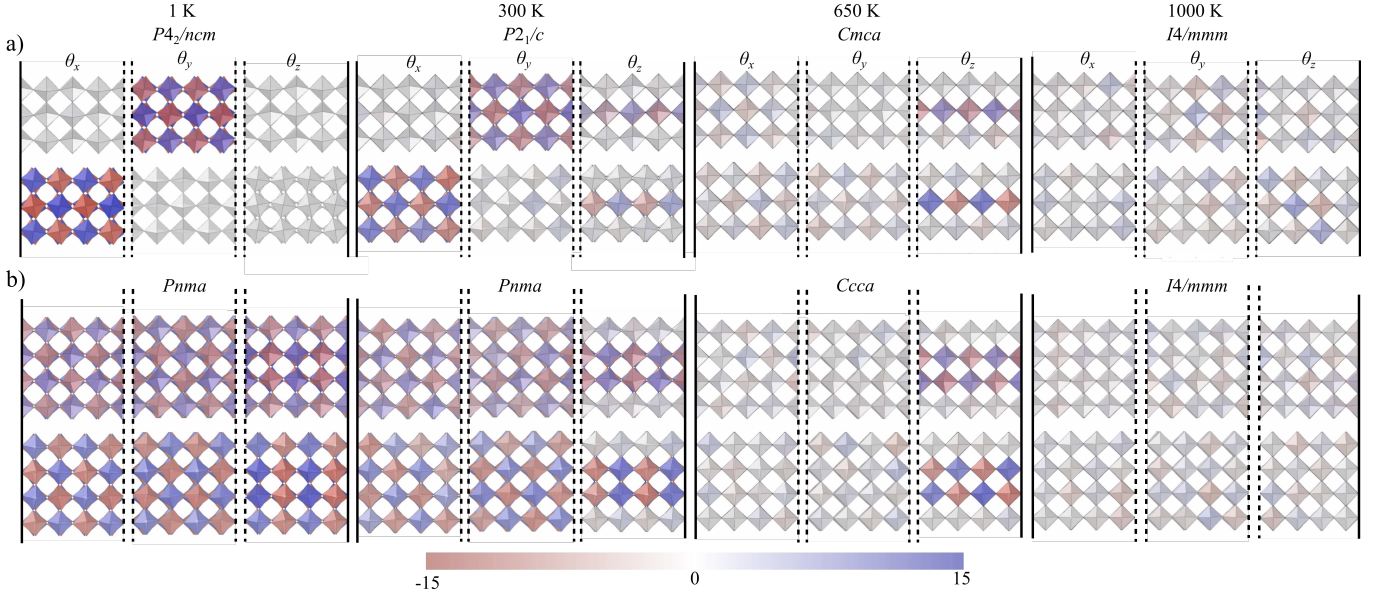


FIG. 4. Snapshots of Euler angles (θ_x , θ_y , θ_z) for $\text{Ba}_{n+1}\text{Zr}_n\text{S}_{3n+1}$ with a) $n = 3$ and b) $n = 4$. The octahedra are colour-coded according to the magnitude of their tilt angles. Solid lines separate the structures by temperature, dashed lines separate the structures by tilt axis. The structures are viewed along the x -axis for θ_x and θ_z , and along the y -axis for θ_y .

tion of temperature for low- n and high- n RP materials in Fig. 5. The ground state amplitude, ranging from 0.35 Å to 0.45 Å is consistent with other compounds where the AX layer (in this case $\text{Ba}^{2+}\text{S}^{2-}$) has no net charge [58]. We note that out-of-plane Ba-displacements within the interior layer(s) are heavily suppressed, and that the average Ba-displacement vector (and net dipole moment) across the slab is zero (see Supplemental Material).

We observe a clear competition between out-of-plane octahedral rotation and rumpling, as has been previously reported for RP materials [58–60]. For $n \geq 4$ the rumpling amplitude increases as the out-of-phase tilting for layers at the rocksalt interface decreases (see Fig. 5b and Supplemental Material). Rumpling reaches a maximum at the point of the surface tilt transition, i.e. the point where the out-of-plane tilts at the rocksalt layer disappears. The inverse coupling is further demonstrated through analysis of the associated phonon modes (Fig. 5c). For large rumpling amplitudes the minimum energy structure corresponds to zero out-of-plane octahedral tilting ($Q_{\psi_z} = 0$), and as the rumpling amplitude decreases the tilt amplitude increases. The competition between rumpling and tilting results from both distortions adjusting A–X distances; out-of-plane octahedral tilting reduces the distance between Ba and S, leading to an over-coordination of the A-site cation when combined with rumpling (see Supplemental Material). Rumpling and its competition with octahedral tilting thus provides an understanding of why surface transitions occur in these materials.

The unusual symmetry-lowering $P4_2/ncm$ to $P2_1/c$ phase transition in $\text{Ba}_4\text{Zr}_3\text{S}_{10}$ is due to the delicate bal-

ance between the in-plane and out-of-plane octahedral tilting coupled with rumpling. In the ground state, the in-plane tilt amplitudes Q_ϕ are large, which suppresses the out-of-plane tilt ψ_z (Fig. 5d). As temperature increases, Q_ϕ decreases, so that the ψ_z tilt becomes energetically favourable, lowering the overall symmetry of the system. The outermost perovskite layers do not tilt due to rumpling at the rocksalt layer. For the $n = 1, 2$ RP materials all layers are rumpled at the rocksalt boundary, so that all out-of-plane octahedral tilts and associated symmetry lowering transitions are suppressed. For $n \geq 4$ the ϕ_z tilt is already active at low temperature, again disallowing the symmetry-lowering transition.

Small changes to perovskite tilt patterns and cation displacements, as observed here, are closely connected to functional properties including band gap, electronic mobility, and defect chemistry. Having a complete picture of the accessible temperature-dependent polymorphs provides the necessary starting point for discovering new materials with target properties, and establishing (layered-)perovskite chalcogenides as a new class of functional materials.

Our simulations reveal a large, diverse set of polymorphs between $n = 1$ to $n = 4$, each exhibiting a range of unexpected behaviour warranting further study: negative thermal expansion along the in-plane lattice parameters for Ba_2ZrS_3 , phase transitions to lower symmetry structures with increasing temperature for Ba_2ZrS_3 and $\text{Ba}_4\text{Zr}_3\text{S}_{10}$, and surface transitions resulting in complex layer-dependent tilt patterns for $n \geq 4$.

Increased octahedral rotations in the ground-state structures lead to perovskite-like structural properties for

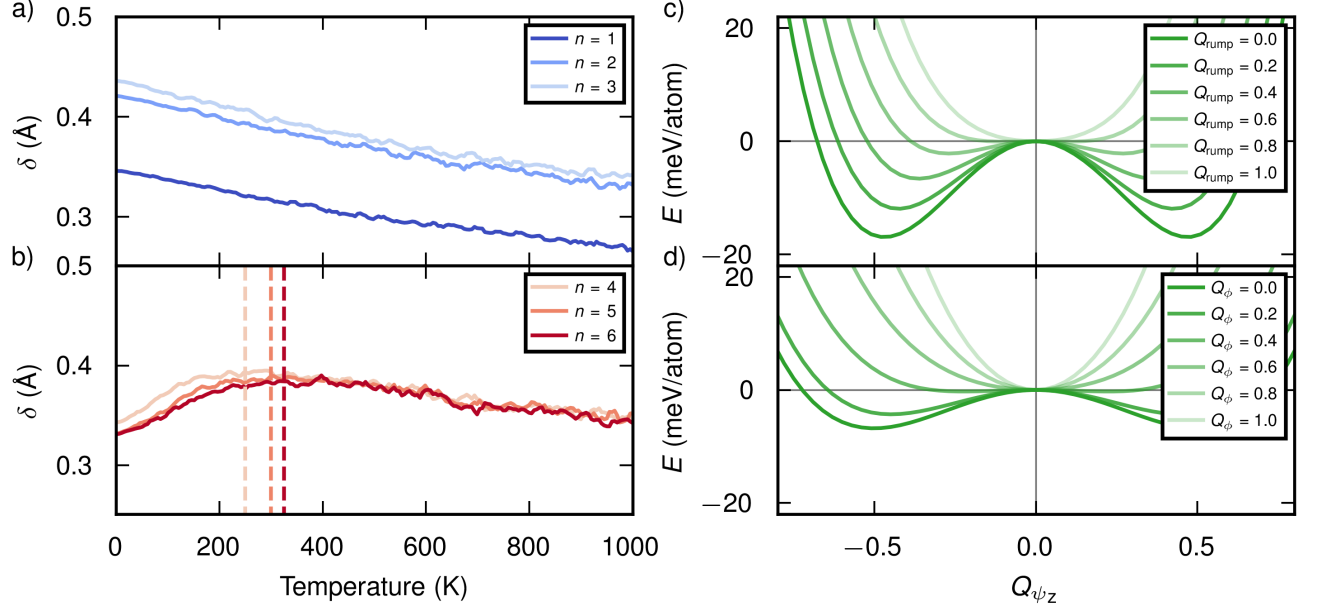


FIG. 5. Rumpling amplitudes (δ) as defined by out-of-plane Ba-cation displacements in the outermost layers of a) $n = 1$ to 3 and b) $n = 4$ to 6 RP phases. Surface transition temperatures are plotted with dashed vertical lines. 1-D potential energy surfaces for out-of-plane tilts in the $n = 3$ RP phase. The landscape is shown for various c) rumpling amplitudes and d) in-plane tilt amplitudes.

high- n RP materials. We find relatively slow convergence ($n \geq 4$) when compared to the structural evolution of the RP oxides [9], and it is this which enables access to a diverse set of polymorphs. This suggests that the suppression of octahedral tilting at low temperature is a design strategy for accessing structures with a broad range of properties and/or advanced functionality. In this case, the suppression of octahedral tilting is associated with increased rumpling at the rocksalt interface, which might be amplified through A-site doping combined with epitaxial growth techniques to induce lateral strain. It might also be engineered in RP chalcogenides with non-centrosymmetric ground states—such as those with Ca on the A-site [21]—for ferroelectric applications.

ACKNOWLEDGMENTS

P.K. is grateful for funding through the Turing Scheme, which facilitated a research visit to Chalmers University of Technology. P.K. also acknowledges support from the UK Engineering and Physical Sciences Research Council (EPSRC) CDT in the Renewable Energy North-east Universities (ReNU) for funding through EPSRC Grant EP/S023836/1. This article is based upon the work from COST Action RenewPV CA21148, supported by COST (European Cooperation in Science and Technology). This work has also been supported by the

Swedish Research Council (Nos. 2020-04935 and 2021-05072) and the Knut and Alice Wallenberg Foundation (No. 2024.0042).

This work used the Oswald High-Performance Computing Facility operated by Northumbria University (UK) and the ARCHER2 UK National Supercomputing Service, through our membership in the UK’s HEC Materials Chemistry Consortium, which is funded by EPSRC (EP/X035859). We are also grateful to the UK Materials and Molecular Modelling Hub for computational resources, which is partially funded by EPSRC (EP/T022213, EP/W032260, and EP/P020194), the National Academic Infrastructure for Supercomputing in Sweden (NAISS) at NSC, PDC, and C3SE, partially funded by the Swedish Research Council through grant agreement no. 2022-06725, as well as the Berzelius resource provided by the Knut and Alice Wallenberg Foundation at NSC.

We thank Kevin Ye and Shanyuan Niu for providing us with the experimental X-ray diffraction patterns. We also thank Kevin, Shanyuan, Emma McCabe, and Nick Bristowe for insightful discussion relating to this work.

DATA AVAILABILITY STATEMENT

The NEP models generated in this study are openly available via Zenodo at <https://doi.org/10.5281/>

zenodo.15829577. The DFT output data has been uploaded to the NOMAD repository at <https://doi.org/10.17172/NOMAD/2025.07.11-1>. A paper-specific repository at https://github.com/NU-CEM/2025_RP_phases contains Python code to reproduce the figures and analysis.

* l.whalley@northumbria.ac.uk

- [1] M. S. B. Hoque, E. R. Hoglund, B. Zhao, D.-L. Bao, H. Zhou, S. Thakur, E. Osei-Agyemang, K. Hattar, E. A. Scott, M. Surendran, J. A. Tomko, J. T. Gaskins, K. Aryana, S. Makarem, A. Alwen, A. M. Hodge, G. Balasubramanian, A. Giri, T. Feng, J. A. Hachtel, J. Ravichandran, S. T. Pantelides, and P. E. Hopkins, *Nature Communications* **16**, 6104 (2025).
- [2] S. Niu, D. Sarkar, K. Williams, Y. Zhou, Y. Li, E. Bianco, H. Huyan, S. B. Cronin, M. E. McConney, R. Haiges, *et al.*, *Chemistry of Materials* **30**, 4882 (2018).
- [3] C. Ming, K. Yang, H. Zeng, S. Zhang, and Y.-Y. Sun, *Material Horizons* **7**, 2985 (2020).
- [4] M. A. Yattoo and S. J. Skinner, *Materials Today: Proceedings* **56**, 3747 (2022).
- [5] J. Kim, J. Mun, C. M. Palomares Garcíá, B. Kim, R. S. Perry, Y. Jo, H. Im, H. G. Lee, E. K. Ko, S. H. Chang, *et al.*, *Nano Letters* **21**, 4185 (2021).
- [6] M. Zhang, C. Pei, Q. Wang, Y. Zhao, C. Li, W. Cao, S. Zhu, J. Wu, and Y. Qi, *Journal of Materials Science & Technology* **185**, 147 (2024).
- [7] M. Markov, L. Alaerts, H. P. C. Miranda, G. Petretto, W. Chen, J. George, E. Bousquet, P. Ghosez, G.-M. Rignanese, and G. Hautier, *Proceedings of the National Academy of Sciences* **118**, e2026020118 (2021).
- [8] G. Clarke, D. Daisenberger, X. Luo, S. Cheong, N. C. Bristowe, and M. S. Senn, *Physical Review B* **109**, 094107 (2024).
- [9] N. Z. Koocher, L.-F. Huang, and J. M. Rondinelli, *Physical Review Materials* **5**, 053601 (2021).
- [10] M. S. Senn, C. A. Murray, X. Luo, L. Wang, F.-T. Huang, S.-W. Cheong, A. Bombardi, C. Ablitt, A. A. Mostofi, and N. C. Bristowe, *Journal of the American Chemical Society* **138**, 5479 (2016), <https://doi.org/10.1021/jacs.5b13192>.
- [11] Y.-Y. Sun, M. L. Agiorgousis, P. Zhang, and S. Zhang, *Nano Letters* **15**, 581 (2015).
- [12] K. V. Sopiha, C. Comparotto, J. A. Márquez, and J. J. Scragg, *Adv. Opt. Mater.* **10**, 2101704 (2022).
- [13] D. Tiwari, O. S. Hutter, and G. Longo, *J. Phys.: Energy* **3**, 034010 (2021).
- [14] R. Jaramillo and J. Ravichandran, *APL Mater.* **7**, 100902 (2019).
- [15] J. W. Choi, B. Shin, P. Gorai, R. L. Hoyer, and R. Palgrave, *Emerging earth-abundant solar absorbers* (2022).
- [16] X. Song, X. Shai, S. Deng, J. Wang, J. Li, X. Ma, X. Li, T. Wei, W. Ren, L. Gao, Y. Fu, H. Wang, and C. Zeng, *The Journal of Physical Chemistry C* **126**, 11751 (2022), <https://doi.org/10.1021/acs.jpcc.2c02286>.
- [17] Z. Yang, Y. Han, Y. Liang, W. Shen, Z. Zhang, C. Fang, Q. Wang, B. Wan, L. Chen, Y. Zhang, *et al.*, *Acta Materialia*, 120156 (2024).
- [18] E. Osei-Agyemang and G. Balasubramanian, *ACS Applied Energy Materials* **3**, 1139 (2019).
- [19] E. Osei-Agyemang, N. Koratkar, and G. Balasubramanian, *Journal of Materials Chemistry C* **9**, 3892 (2021).
- [20] Y. Wu, Y. Chen, Z. Fang, Y. Ding, Q. Li, K. Xue, H. Shao, H. Zhang, and L. Zhou, *The Journal of Physical Chemistry Letters* **14**, 11465 (2023).
- [21] Y. Zhang, T. Shimada, T. Kitamura, and J. Wang, *The Journal of physical chemistry letters* **8**, 5834 (2017).
- [22] H. Wang, G. Gou, and J. Li, *Nano Energy* **22**, 507 (2016).
- [23] X. Wu, W. Gao, J. Chai, C. Ming, M. Chen, H. Zeng, P. Zhang, S. Zhang, and Y.-Y. Sun, *Science China Materials* **64**, 2976 (2021).
- [24] Z. Yuan, D. Dahliah, R. Claes, A. Pike, D. P. Fenning, G.-M. Rignanese, and G. Hautier, *PRX Energy* **3**, 033008 (2024).
- [25] Y. Jiang, H. K. D. Le, L. Verbitsky, H. DeVyldere, A. M. Oddo, B. Pan, H.-g. Song, C. Zhu, H. Zhu, M. C. Scott, and P. Yang, *Nano Letters* **25**, 7029 (2025), pMID: 40249145, <https://doi.org/10.1021/acs.nanolett.5c00815>.
- [26] R. S. Nielsen, Ángel Labordet Álvarez, Y. Tomm, G. Gurieva, A. Ortega-Guerrero, J. Breternitz, L. Bastonero, N. Marzari, C. A. Pignedoli, S. Schorr, and M. Dimitrievska, *BaZrS₃ Lights Up: The Interplay of Electrons, Photons, and Phonons in Strongly Luminescent Single Crystals* (2025), arXiv:2503.16180 [cond-mat.mtrl-sci].
- [27] Y. Nishigaki, T. Nagai, M. Nishiwaki, T. Aizawa, M. Kozawa, K. Hanzawa, Y. Kato, H. Sai, H. Hiramatsu, H. Hosono, *et al.*, *Solar Rrl* **4**, 1900555 (2020).
- [28] Y.-C. Hung, J. Fetting, and B. Eichhorn, *Crystal Structure Communications* **53**, 827 (1997).
- [29] M. Saeki, Y. Yajima, and M. Onoda, *Journal of Solid State Chemistry* **92**, 286 (1991).
- [30] B.-H. Chen, B. Eichhorn, and W. Wong-Ng, *Crystal Structure Communications* **50**, 161 (1994).
- [31] S. Niu, J. Milam-Guerrero, Y. Zhou, K. Ye, B. Zhao, B. C. Melot, and J. Ravichandran, *Journal of Materials Research* **33**, 4135 (2018).
- [32] B.-H. Chen, W. Wong-Ng, and B. W. Eichhorn, *Journal of Solid State Chemistry* **103**, 75 (1993).
- [33] P. Kayastha, E. Fransson, P. Erhart, and L. Whalley, *The Journal of Physical Chemistry Letters* **16**, 2064 (2025).
- [34] K. Aleksandrov, *Crystallography Reports* **40** (1995).
- [35] Z. Fan, Z. Zeng, C. Zhang, Y. Wang, K. Song, H. Dong, Y. Chen, and T. Ala-Nissila, *Physical Review B* **104**, 104309 (2021).
- [36] Z. Fan, *Journal of Physics: Condensed Matter* **34**, 125902 (2022).
- [37] Z. Fan, Y. Wang, P. Ying, K. Song, J. Wang, Y. Wang, Z. Zeng, K. Xu, E. Lindgren, J. M. Rahm, A. J. Gabourie, J. Liu, H. Dong, J. Wu, Y. Chen, Z. Zhong, J. Sun, P. Erhart, Y. Su, and T. Ala-Nissila, *The Journal of Chemical Physics* **157**, 114801 (2022).
- [38] J. Heyd, G. E. Scuseria, and M. Ernzerhof, *The Journal of Chemical Physics* **118**, 8207 (2003).
- [39] V. Blum, R. Gehrke, F. Hanke, P. Havu, V. Havu, X. Ren, K. Reuter, and M. Scheffler, *Computer Physics Communications* **180**, 2175 (2009).
- [40] F. Knoop, T. Purcell, M. Scheffler, and C. Carbogno, *The Journal of Open Source Software* **5** (2020).
- [41] See supplemental material at [url will be inserted by publisher] for further calculation details and analysis (2025).

- [42] A. H. Larsen, J. J. Mortensen, J. Blomqvist, I. E. Castelli, R. Christensen, M. Dulak, J. Friis, M. N. Groves, B. Hammer, C. Hargus, E. D. Hermes, P. C. Jennings, P. B. Jensen, J. Kermode, J. R. Kitchin, E. L. Kolsbjerg, J. Kubal, K. Kaasbjerg, S. Lysgaard, J. B. Maronsson, T. Maxson, T. Olsen, L. Pastewka, A. Peterson, C. Rostgaard, J. Schiøtz, O. Schütt, M. Strange, K. S. Thygesen, T. Vegge, L. Vilhelmsen, M. Walter, Z. Zeng, and K. W. Jacobsen, *Journal of Physics: Condensed Matter* **29**, 273002 (2017).
- [43] E. Lindgren, M. Rahm, E. Fransson, F. Eriksson, N. Österbacka, Z. Fan, and P. Erhart, *Journal of Open Source Software* **9**, 6264 (2024).
- [44] J. P. Perdew, A. Ruzsinszky, G. I. Csonka, O. A. Vydrov, G. E. Scuseria, L. A. Constantin, X. Zhou, and K. Burke, *Physical Review Letters* **100**, 136406 (2008).
- [45] A. Togo, *Journal of the Physical Society of Japan* **92**, 012001 (2023).
- [46] A. Togo, K. Shinohara, and I. T. and, *Science and Technology of Advanced Materials: Methods* **4**, 2384822 (2024).
- [47] A. Stukowski, *Modelling and Simulation in Materials Science and Engineering* **18**, 015012 (2009).
- [48] F. Eriksson, E. Fransson, and P. Erhart, *Advanced Theory and Simulations* **2**, 1800184 (2019).
- [49] E. Fransson, J. Wiktor, and P. Erhart, *The Journal of Physical Chemistry C* **127**, 13773 (2023).
- [50] E. Fransson, J. Wiktor, and P. Erhart, *ACS Energy Letters* **9**, 3947 (2024).
- [51] E. Fransson, P. Rosander, F. Eriksson, J. M. Rahm, T. Tadano, and P. Erhart, *Communications Physics* **6**, 173 (2023).
- [52] K. S. Aleksandrov, B. V. Beznosikov, and S. V. Misyul, *Physica Status Solidi (a)* **104**, 529 (1987).
- [53] C. Ablitt, S. Craddock, M. S. Senn, A. A. Mostofi, and N. C. Bristowe, *npj Computational Materials* **3**, 10.1038/s41524-017-0040-0 (2017).
- [54] N. Z. Koocher, A. B. Altman, R. A. Klein, C. D. Malliakas, S. D. Jacobsen, D. E. Freedman, and J. M. Rondinelli, *Inorganic Chemistry* **64**, 10761 (2025), pMID: 40413650, <https://doi.org/10.1021/acs.inorgchem.5c00314>.
- [55] S. Niu, B. Zhao, K. Ye, E. Bianco, J. Zhou, M. E. McConney, C. Settens, R. Haiges, R. Jaramillo, and J. Ravichandran, *Journal of Materials Research* **34**, 3819 (2019).
- [56] Perez-Mato, J.M., Aroyo, M.I., and Orobengoa, D., *EPJ Web of Conferences* **22**, 00008 (2012).
- [57] M. H. Christensen, P. P. Orth, B. M. Andersen, and R. M. Fernandes, *Phys. Rev. Lett.* **121**, 057001 (2018).
- [58] Y. Zhang, J. Wang, and P. Ghosez, *Phys. Rev. Lett.* **125**, 157601 (2020).
- [59] T. Birol, N. A. Benedek, and C. J. Fennie, *Physical Review Letters* **107**, 257602 (2011).
- [60] G. Stone, C. Ophus, T. Birol, J. Ciston, C.-H. Lee, K. Wang, C. J. Fennie, D. G. Schlom, N. Alem, and V. Gopalan, *Nature Communications* **7**, 12572 (2016).

Supporting Information:

Diverse polymorphism in Ruddlesden-Popper chalcogenides

Prakriti Kayastha¹, Erik Fransson², Paul Erhart², and Lucy Whalley¹

¹ *Department of Physics, Chalmers University of Technology, SE-41296, Gothenburg, Sweden*

¹ *Department of Mathematics, Physics and Electrical Engineering, Northumbria University, Newcastle upon Tyne, NE1 8QH, United Kingdom*

July 16, 2025

Contents

Methods	2
Neuroevolution potential method	2
Density functional theory calculations	2
Molecular dynamics simulations	2
Validation of NEP	4
Ground state energies	6
Projection onto octahedral tilt modes	8
Tilt angle heatmaps	16
Octahedral tilt angles for $n = 1$ to $n = 4$ RP phases	20
Finite-temperature polymorphs	21
A-site displacements	22
X-ray diffraction	25
Supplemental References	27

Methods

Neuroevolution potential method

An iterative strategy was employed to construct the neuroevolution potential outlined in Ref. 49. The GPUMD package^{35–37} (version 3.9.5) was used to build the neuroevolution potential (NEP) model and run the molecular dynamics (MD) simulations. The ASE⁴² and CALORINE⁴³ packages were used to prepare the training structures, set up MD simulations and post-process the results. Random displacements were generated using the HIPHIVE package⁴⁸.

The initial training set contains strained primitive structures and rattled supercells of the perovskite and the $n = 1$ to 6 RP phases. The different phases considered for the perovskite are described in Ref. 33.

The training structures include ideal, distorted, and deformed unit cells and supercells of Ruddlesden-Popper materials for $n = 1$ to $n = 6$, along with the 33 tilt pattern structures defined by Aleksandrov for $n = 1$ to $n = 10$. Molecular dynamics (MD) structures were included for temperatures up to 1000 K. The final training set consists of 1375 structures.

The initial model was trained using density functional theory (DFT) data generated with the PBEsol exchange-correlation functional⁴⁴. For each structure in the training set, formation energy (relative to the elemental phases), atomic forces and stress tensors were evaluated using DFT. This model was then used to run MD simulations in the NPT ensemble, over a temperature range of 1 K to 1000 K with varying supercell sizes, containing between 20 and 500 atoms. The model was retrained after adding snapshots from randomly selected structures from the MD runs.

On the final training set, we used higher accuracy HSE06 functional⁷ to calculate energies, forces, and stress tensors. Stress tensors for structures containing more than 60 atoms were not evaluated as the memory requirements for these calculations were prohibitively large.

Density functional theory calculations

Formation energies, forces, and stress tensors used in the training set were calculated using the all-electron numeric atom-centered orbital code FHI-aims³⁹. Due to large memory requirements, the stress tensors are not calculated for structures larger than 60 atoms in the unit cell. FHI-vibes⁴⁰ was used for pre and post-processing of DFT data. All DFT calculations used the *light* basis set and a Monkhorst-Pack k -point mesh with a minimum k -spacing of $0.2/\text{\AA}$. For single-point calculations, the charge density was converged to an accuracy of 10^{-6} , forces to 10^{-5} eV/\AA , and stresses to 10^{-4} eV/\AA^3 . Geometry relaxations were carried out using the symmetry-constrained relaxation scheme as implemented in ASE⁴², until the maximal force component was below 10^{-3} eV/\AA . Harmonic phonon dispersions at 0 K using the PHONOPY package⁴⁵ with a $2 \times 2 \times 2$ supercell and a 0.01 \AA displacement distance. Forces for these phonon calculations were converged below 10^{-3} eV/\AA .

Molecular dynamics simulations

To perform the heating runs, the MD simulations were carried out using the GPUMD software⁷ with a timestep of 1 fs. The ASE⁴² and calorine⁴³ packages were used to set up the MD simulations and post-process the results. Heating and cooling simulations were run in the NPT ensemble between 0 K to 1200 K for 50 ns using a supercell consisting of about 40 000 atoms. The potential energy and lattice parameters were recorded every 100 fs to discern phase transitions.

Additional cooling simulations were performed for both the Ruddlesden-Popper series and the perovskite phase, starting from the ideal $I4/mmm$ and $Pm\bar{3}m$ structures, respectively. For RP phases with $n \geq 6$ and for the perovskite, we observe significant hysteresis during cooling, where the system becomes kinetically trapped in a metastable phase and does not undergo the expected first-order transition, persisting in this state down to 0 K.

The heat capacities across the different phase transitions were calculated by fitting the potential energy and the temperature data from MD to an analytical expression and then taking its derivative as done in Ref. 50. The analytical function for the energy is a polynomial in temperature for each phase, splined together with an S-like error-function, where the location and width of this splining are also fit parameters. This ensures that the analytical form can capture sharp discontinuous changes in

the energy as well as broad continuous changes in the energy across phase transitions, and therefore allows a more reliable estimate of the heat capacity to be obtained compared to direct numerical differentiation.

To identify the finite-temperature polymorphs stabilized during heating, atomic displacements were projected onto the in-phase and out-of-phase octahedral tilt eigenmodes of the ideal $I4/mmm$ phase. These mode projections were evaluated separately for the two inequivalent slabs within the Ruddlesden-Popper structure. For the perovskite phase, projections were instead based on the phonon eigenvectors of the $Pm\bar{3}m$ structure, following the methodology in Refs. 51. The space groups of RP structures exhibiting suppressed surface-layer tilting were assigned by constructing idealized structural models with the same octahedral tilt as observed in MD, and evaluating them with SPGLIB⁴⁶.

Structural visualizations and analysis were performed using the OVITO package⁴⁷.

Validation of NEP

The final model achieved root mean squared errors of 1.8 meV/atom for formation energies, 68.4 meV/Å for atomic forces, and 26.1 meV/Å³/atom for virial stresses. Loss curves, root mean square errors and parity plots are provided below.

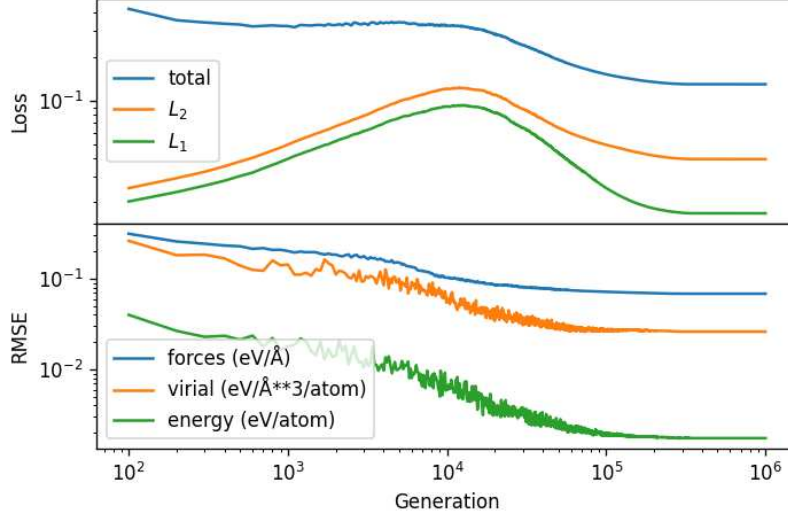


Figure S1: Loss curves and root mean square errors (RMSE) of energies, forces, and virials for the full model.

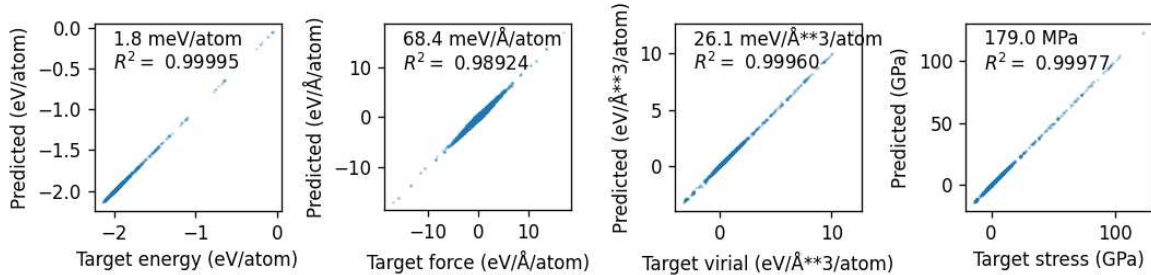


Figure S2: Parity plots for the full model. Structures for which the stress tensors have not been evaluated with DFT are not included in the virial and stress tensor plots.

The 0 K harmonic phonon spectra for Ruddlesden-Popper materials in the high-temperature phase are displayed below. The solid blue lines correspond to phonons generated by evaluating forces from the NEP model, and the dashed black lines are phonons generated by evaluating forces from DFT. The largest discrepancies correspond to high-frequency modes associated with the sulfur species.²⁰

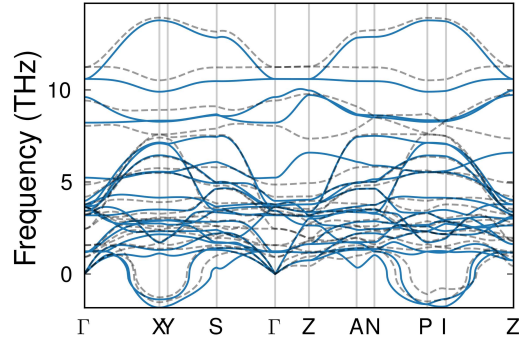


Figure S3: Phonons of the $n = 1$ RP in the $I4/mmm$ phase using NEP (solid blue) and DFT (dashed black)

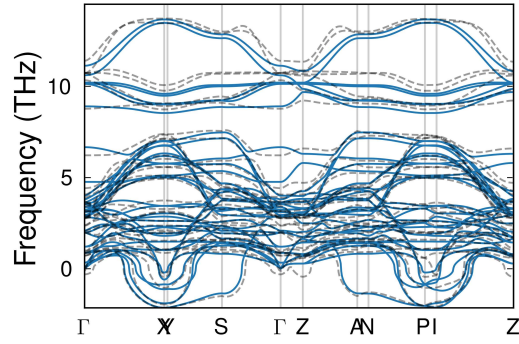


Figure S4: Phonons of the $n = 2$ RP in the $I4/mmm$ phase using NEP (solid blue) and DFT (dashed black)

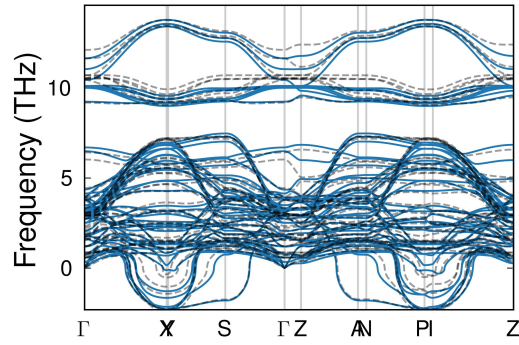


Figure S5: Phonons of the $n = 3$ RP in the $I4/mmm$ phase using NEP (solid blue) and DFT (dashed black)

Ground state energies

NEP-calculated energies of the 33 unique octahedral tilt patterns, after geometry relaxation with constrained symmetry. The tilt patterns are given in Aleksandrov notation (see main text). The energies are specified relative to the ground state (which is indicated in bold). Some tilt patterns have the same energy. In this case, the lower-symmetry phase is unstable and has relaxed to the higher symmetry phase.

space group	Slab I Slab II	$n = 1$	$n = 3$	$n = 5$
<i>I4/mmm</i>	000 000	0.00719	0.01314	0.01909
<i>Cmca</i>	00 ψ 00 ψ	0.00719	0.00516	0.00737
<i>P4/mbm</i>	00 ψ 000	0.00719	0.01030	0.01451
<i>Pbam</i>	00 ψ_{z_1} 00 ψ_{z_2}	0.00719	0.00516	0.00737
<i>Cmca</i>	00 ϕ 00 ϕ	0.00719	0.00516	0.00467
<i>P4/mbm</i>	00 ϕ 000	0.00719	0.01030	0.01328
<i>Pbam</i>	00 ϕ_{z_1} 00 ϕ_{z_2}	0.00719	0.00516	0.00467
<i>P4₂/nnm</i>	ϕ 00 0 ϕ 0	0.00456	0.00245	0.00441
<i>Cccm</i>	$\phi\phi$ 0 $\phi\phi$ 0	0.00486	0.00416	0.00538
<i>Pnnn</i>	$\phi_{x_1}\phi_{y_2}$ 0 $\phi_{x_2}\phi_{y_1}$ 0	0.00456	0.00245	0.00437
<i>P4₂/ncm</i>	ϕ 00 0 ϕ 0	0.00000	0.00000	0.00287
<i>Cmca</i>	$\phi\phi$ 0 $\phi\bar{\phi}$ 0	0.00082	0.00194	0.00399
<i>Pccn</i>	$\phi_{x_1}\phi_{y_2}$ 0 $\phi_{x_2}\phi_{y_1}$ 0	0.00000	0.00000	0.00284
<i>P2₁/c</i>	ϕ 0 ψ 0 $\phi\psi$	0.00000	0.00000	0.00005
<i>P2₁/c</i>	ϕ 0 ϕ 0 $\phi\phi$	0.00000	0.00000	0.00286
<i>P2/c</i>	ϕ 0 ψ 0 $\phi\psi$	0.00456	0.00245	0.00114
<i>P2/c</i>	ϕ 0 ϕ 0 $\phi\phi$	0.00456	0.00245	0.00492
<i>C2/m</i>	ϕ 0 ψ 0 ϕ 0	0.00000	0.00000	0.00287
<i>C2/m</i>	ϕ 0 ϕ 0 ϕ 0	0.00000	0.00000	0.00287
<i>C2/m</i>	ϕ 0 ψ 0 ϕ 0	0.00000	0.00245	0.00439
<i>C2/m</i>	ϕ 0 ϕ 0 ϕ 0	0.00000	0.00245	0.00439
<i>C2/c</i>	$\phi\phi\psi$ $\phi\phi\psi$	0.00486	0.00191	0.00114
<i>C2/c</i>	$\phi\phi\phi$ $\phi\phi\phi$	0.00486	0.00191	0.00466
<i>Pccn</i>	$\phi\phi\psi$ $\phi\phi\bar{\psi}$	0.00486	0.00192	0.00114
<i>Pccn</i>	$\phi\phi\phi$ $\phi\phi\bar{\phi}$	0.00486	0.00192	0.00467
<i>Pbca</i>	$\phi\phi\psi$ $\phi\phi\psi$	0.00082	0.00013	0.00005
<i>Pbca</i>	$\phi\phi\phi$ $\phi\phi\phi$	0.00082	0.00013	0.00371
<i>P2₁/c</i>	$\phi\phi\psi$ $\phi\phi\bar{\psi}$	0.00082	0.00005	0.00000
<i>P2₁/c</i>	$\phi\phi\phi$ $\phi\phi\bar{\phi}$	0.00082	0.00005	0.00367
<i>P2₁/c</i>	$\phi\phi\psi$ $\phi\phi$ 0	0.00486	0.00192	0.00114
<i>P2₁/c</i>	$\phi\phi\psi$ $\phi\phi$ 0	0.00082	0.00013	0.00005
<i>P2₁/c</i>	$\phi\phi\phi$ $\phi\phi$ 0	0.00486	0.00191	0.00302
<i>P2₁/c</i>	$\phi\phi\phi$ $\phi\phi$ 0	0.00082	0.00005	0.00195

Table S1: Space groups, tilt patterns, and NEP-calculated energies of RP structures with an odd number of layers within each slab. Energies are given in eV/atom and referenced to the ground state.

space group	Slab I Slab II	$n = 2$	$n = 4$	$n = 6$
<i>I4/mmm</i>	000 000	0.01054	0.01661	0.02089
<i>Cmca</i>	00 ψ 00 ψ	0.01034	0.00921	0.00798
<i>P4/mbm</i>	00 ψ 000	0.01054	0.01279	0.01575
<i>Pbam</i>	00 ψ_{z_1} 00 ψ_{z_2}	0.01034	0.00921	0.00798
<i>Ccce</i>	00 ϕ 00 ϕ	0.00826	0.00482	0.00457
<i>P4/nbm</i>	00 ϕ 000	0.01032	0.01202	0.01419
<i>Pban</i>	00 ϕ_{z_1} 00 ϕ_{z_2}	0.00826	0.00482	0.00457
<i>P4₂/mnm</i>	ϕ 00 0 ϕ 0	0.00000	0.00166	0.00373
<i>Cmcm</i>	$\phi\phi$ 0 $\phi\phi$ 0	0.00200	0.00315	0.00457
<i>Pnnm</i>	$\phi_{x_1}\phi_{y_2}$ 0 $\phi_{x_2}\phi_{y_1}$ 0	0.00000	0.00166	0.00360
<i>P4₂/mcm</i>	ϕ 00 0 ϕ 0	0.00340	0.00356	0.00502
<i>Cmma</i>	$\phi\phi$ 0 $\bar{\phi}\bar{\phi}$ 0	0.00496	0.00487	0.00573
<i>Pccm</i>	$\phi_{x_1}\phi_{y_2}$ 0 $\bar{\phi}_{x_2}\bar{\phi}_{y_1}$ 0	0.00340	0.00356	0.00488
<i>Pma2</i>	ϕ 0 ψ 0 $\phi\psi$	0.00340	0.00141	0.00095
<i>P2/c</i>	ϕ 0 ϕ 0 $\bar{\phi}$	0.00340	0.00354	0.00523
<i>Pmn2₁</i>	ϕ 0 ψ 0 $\bar{\phi}\psi$	0.00000	0.00006	0.00004
<i>P2₁/c</i>	ϕ 0 ϕ 0 $\phi\phi$	0.00000	0.00166	0.00431
<i>Amm2</i>	ϕ 0 ψ 0 ϕ 0	0.00340	0.00356	0.00500
<i>C2/m</i>	ϕ 0 ϕ 0 ϕ 0	0.00340	0.00355	0.00520
<i>Amm2</i>	ϕ 0 ψ 0 $\bar{\phi}$ 0	0.00000	0.00166	0.00371
<i>C2/m</i>	ϕ 0 ϕ 0 $\bar{\phi}$ 0	0.00000	0.00166	0.00408
<i>Cmc2₁</i>	$\phi\phi\psi$ $\phi\phi\psi$	0.00200	0.00006	0.00004
<i>C2/c</i>	$\phi\phi\phi$ $\phi\phi\phi$	0.00200	0.00248	0.00401
<i>Pnma</i>	$\phi\phi\psi$ $\phi\phi\bar{\psi}$	0.00200	0.00000	0.00000
<i>Pbcn</i>	$\phi\phi\phi$ $\phi\phi\bar{\phi}$	0.00200	0.00254	0.00405
<i>Pbcm</i>	$\phi\phi\psi$ $\bar{\phi}\bar{\phi}\psi$	0.00496	0.00141	0.00096
<i>Pcca</i>	$\phi\phi\phi$ $\bar{\phi}\bar{\phi}\bar{\phi}$	0.00496	0.00394	0.00479
<i>Abm2</i>	$\phi\phi\psi$ $\bar{\phi}\bar{\phi}\bar{\psi}$	0.00496	0.00141	0.00095
<i>P2/c</i>	$\phi\phi\phi$ $\bar{\phi}\bar{\phi}\bar{\phi}$	0.00496	0.00392	0.00479
<i>Pmc2₁</i>	$\phi\phi\psi$ $\phi\phi$ 0	0.00200	0.00006	0.00004
<i>Pmc2₁</i>	$\phi\phi\psi$ $\bar{\phi}\bar{\phi}$ 0	0.00496	0.00141	0.00095
<i>P2/c</i>	$\phi\phi\phi$ $\phi\phi$ 0	0.00200	0.00248	0.00310
<i>P2/c</i>	$\phi\phi\phi$ $\bar{\phi}\phi$ 0	0.00496	0.00392	0.00399

Table S2: Space groups, tilt patterns, and NEP-calculated energies of RP structures with an even number of layers within each slab. Energies are given in eV/atom and referenced to the ground state.

Projection onto octahedral tilt modes

Projection of the molecular dynamic trajectories onto the ϕ (out-of-phase) and ψ (in-phase) octahedral tilt modes in the heating and cooling runs of the $n = 1$ to 8 RP phases. The tilt components are resolved along the x , y , and z directions for each slab, which is identified by subscript index. The sign of the projection amplitudes Q are used to determine the relative tilt directions between slabs, with opposite tilt directions denoted with an overbar in Aleksandrov notation.

For $n = 1, 2, 3$ the heating and cooling runs produce identical mode projection results, apart from sometimes an arbitrary flip of the sign of the mode coordinates. However, for $n = 4$ and above in the cooling runs sometimes one does not achieve perfect long-range ordering between the slabs and thus the global mode coordinate (averaged over all slabs) can take on different values or sometimes be zero while the structure still is tilted and looks similar to the structure of the heating run.

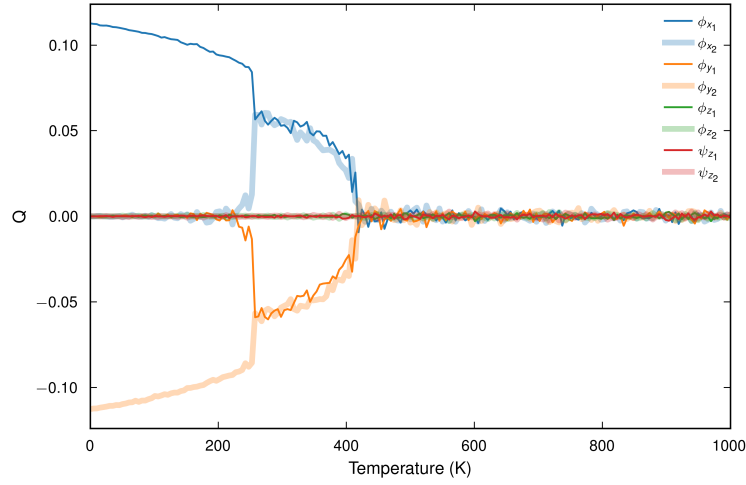


Figure S6: Mode projections in the heating run for the $n = 1$ RP phase.

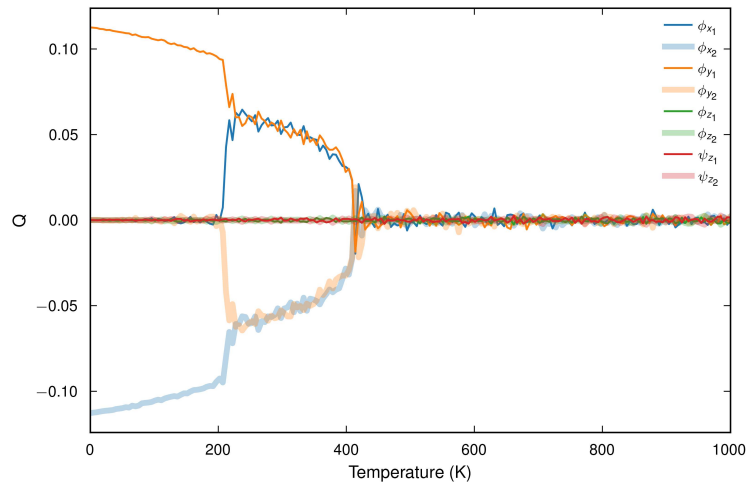


Figure S7: Mode projections in the cooling run for the $n = 1$ RP phase.

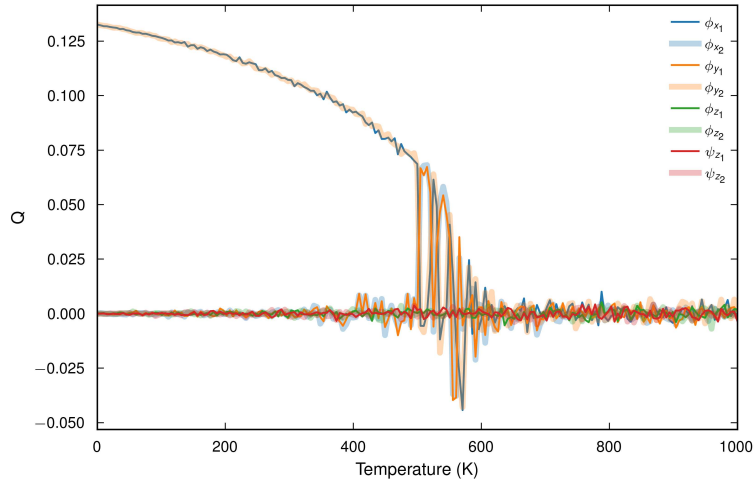


Figure S8: Mode projections in the heating run for the $n = 2$ RP phase.

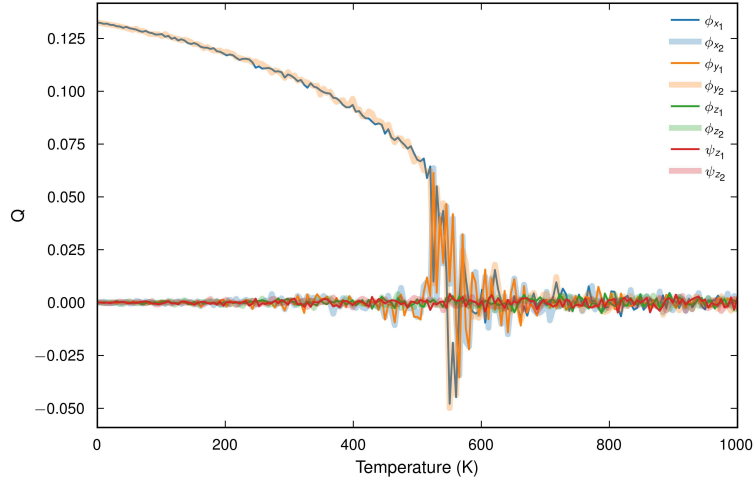


Figure S9: Mode projections in the cooling run for the $n = 2$ RP phase.

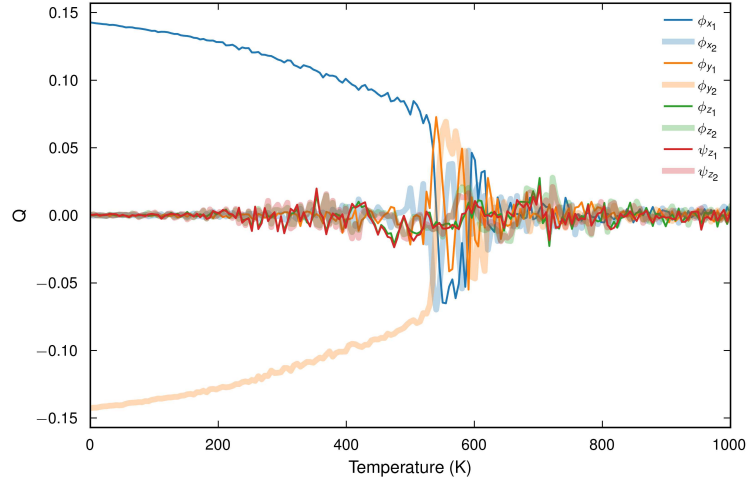


Figure S10: Mode projections in the heating run for the $n = 3$ RP phase.

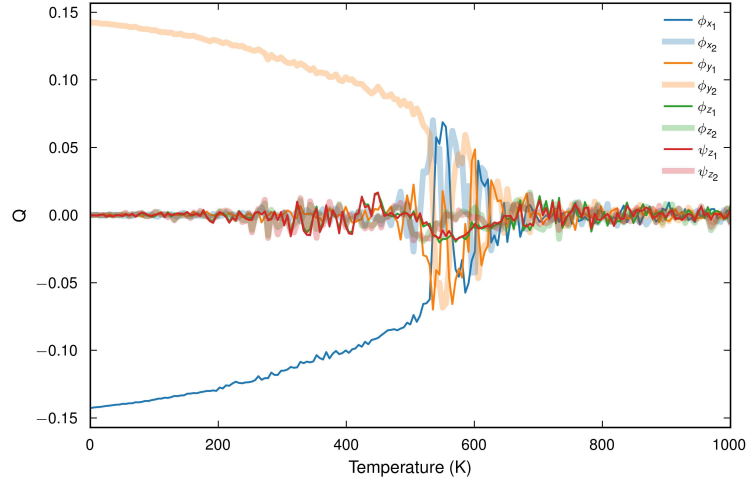


Figure S11: Mode projections in the cooling run for the $n = 3$ RP phase.

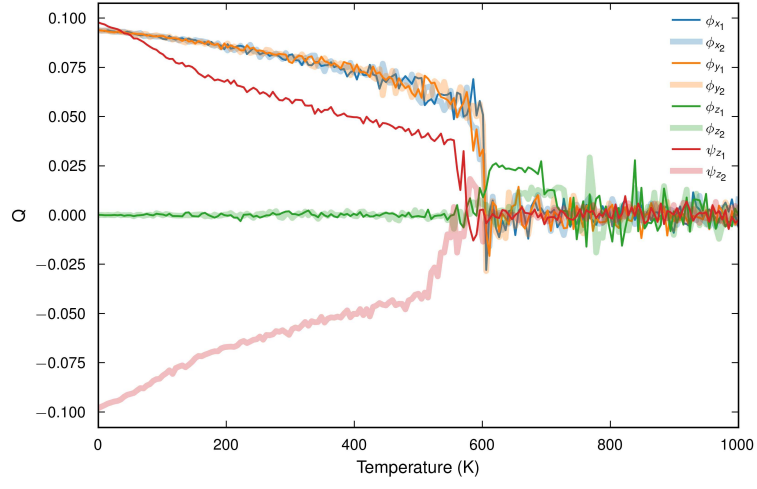


Figure S12: Mode projections in the heating run for the $n = 4$ RP phase.

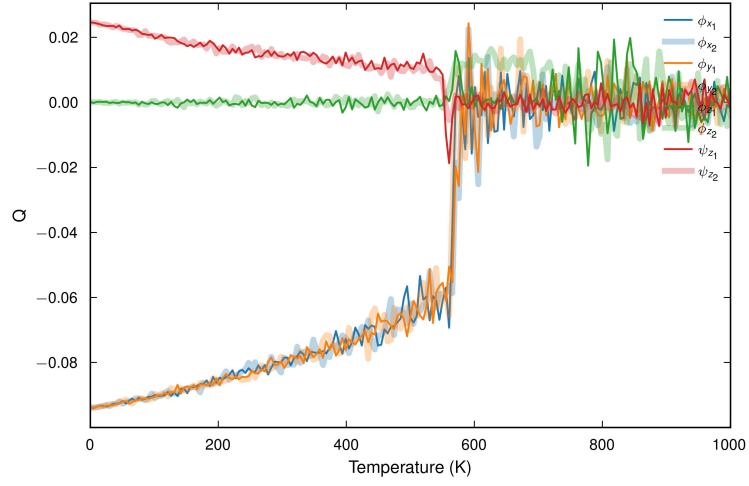


Figure S13: Mode projections in the cooling run for the $n = 4$ RP phase.

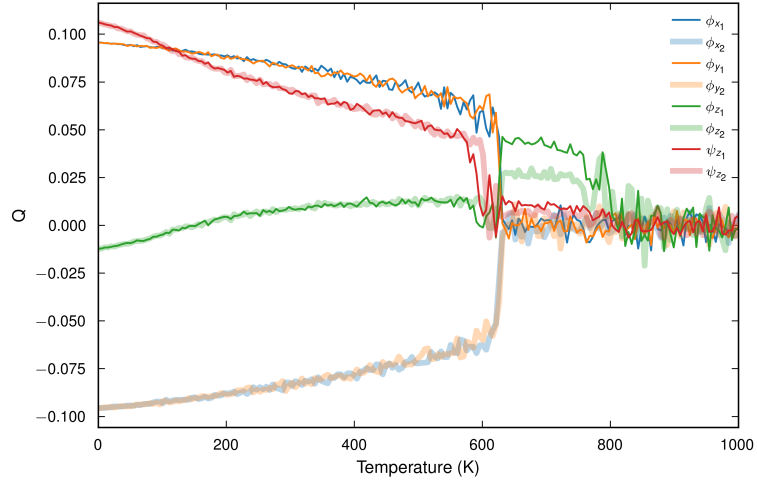


Figure S14: Mode projections in the heating run for the $n = 5$ RP phase.

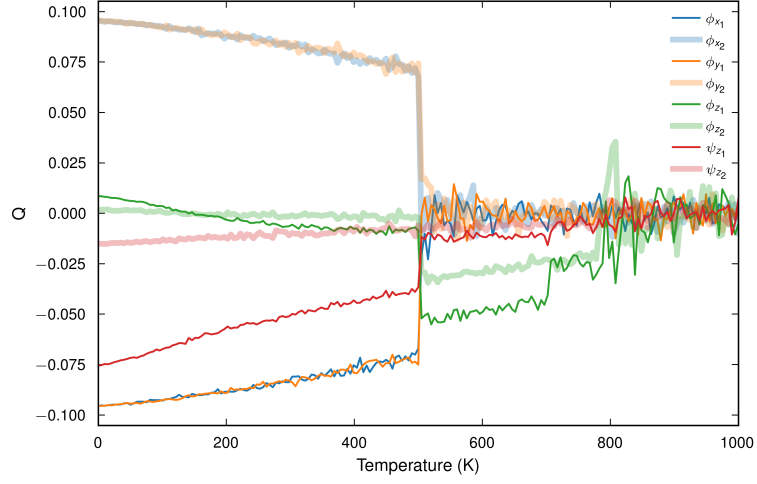


Figure S15: Mode projections in the cooling run for the $n = 5$ RP phase.

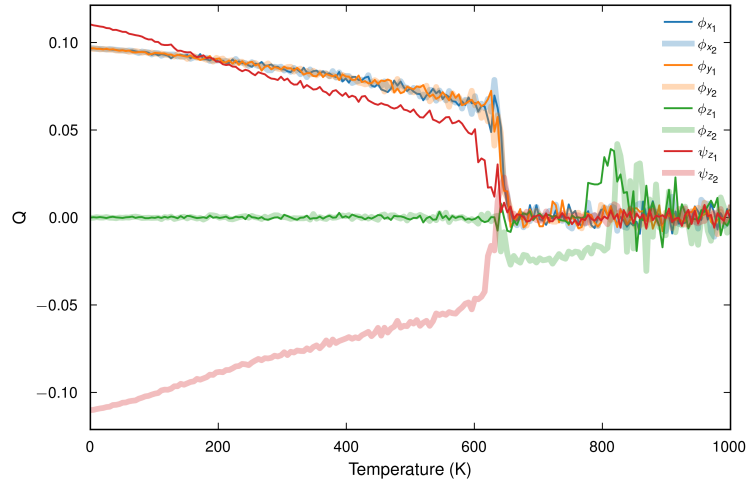


Figure S16: Mode projections in the heating run for the $n = 6$ RP phase.

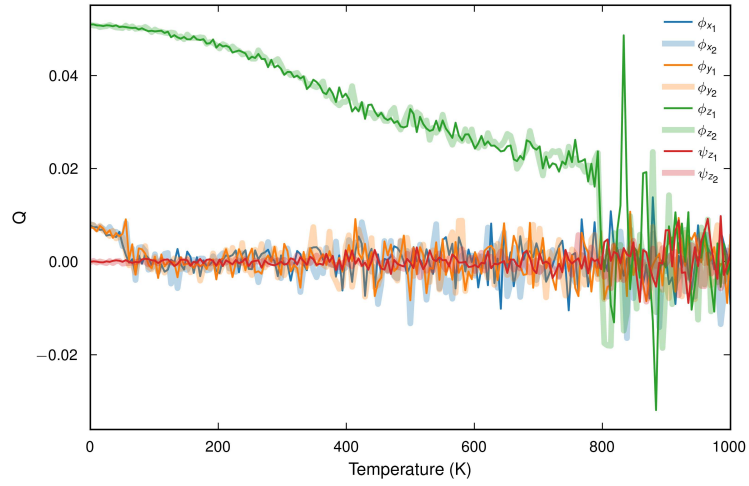


Figure S17: Mode projections in the cooling run for the $n = 6$ RP phase.

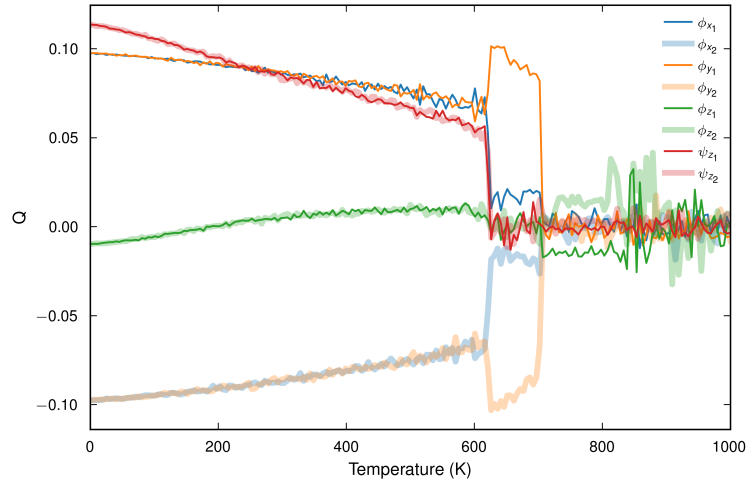


Figure S18: Mode projections in the heating run for the $n = 7$ RP phase.

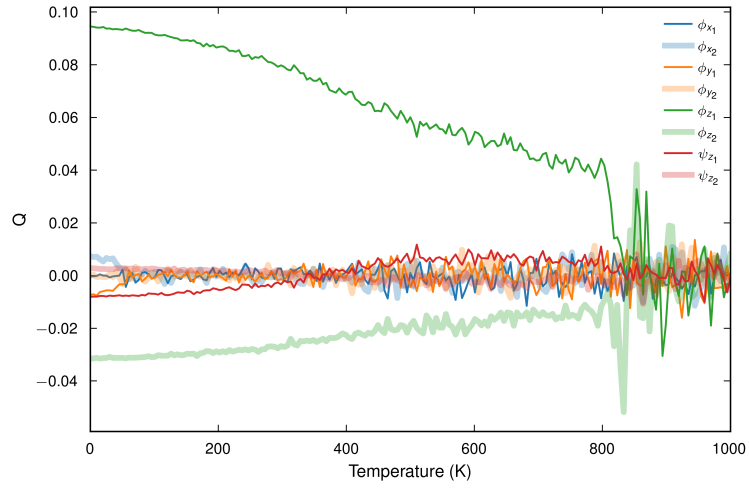


Figure S19: Mode projections in the cooling run for the $n = 7$ RP phase.

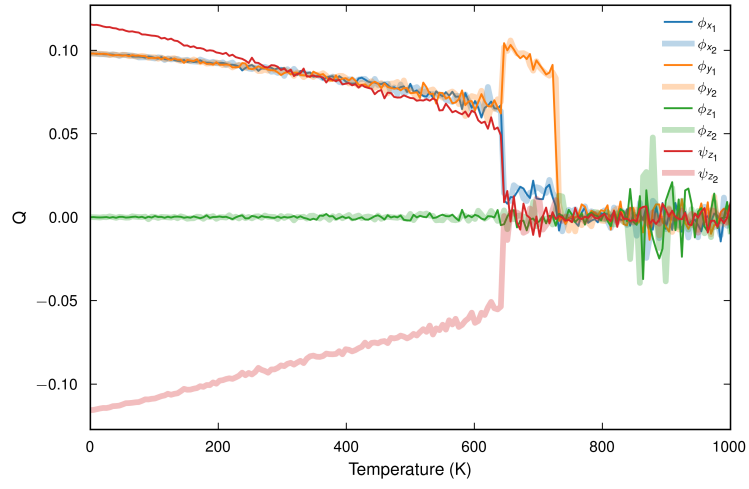


Figure S20: Mode projections in the heating run for the $n = 8$ RP phase.

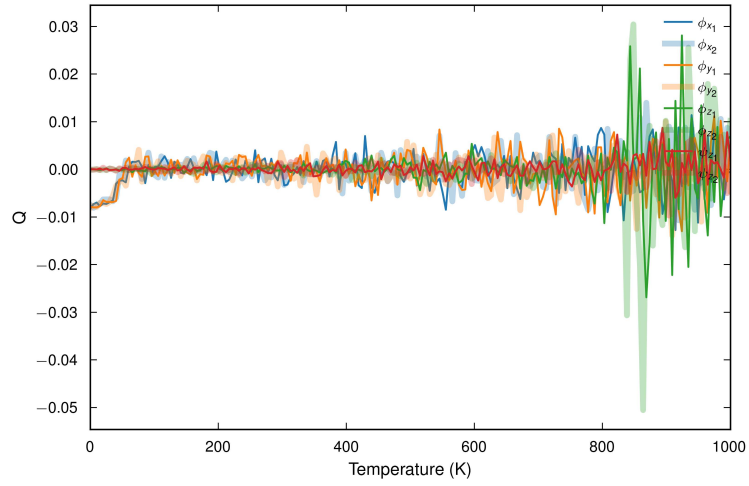


Figure S21: Mode projections in the cooling run for the $n = 8$ RP phase.

Tilt angle heatmaps

Layer-by-layer Euler angles (θ_x , θ_y , θ_z) of the ZrS_6 octahedra in heating runs of the $n = 1$ to 6 RP phases.

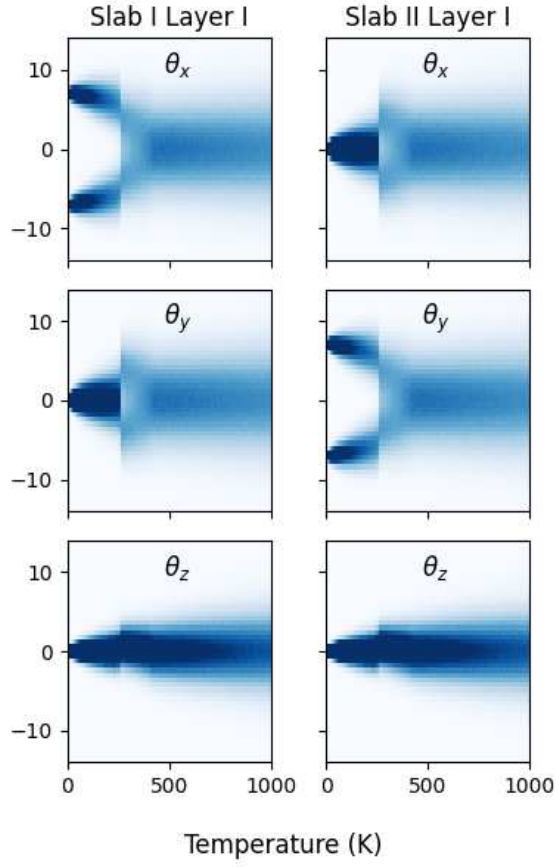


Figure S22: Euler angles of the $n = 1$ RP phase

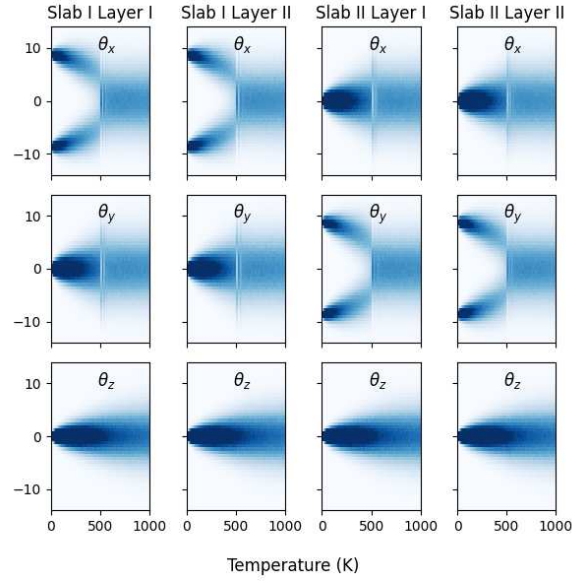


Figure S23: Euler angles of the $n = 2$ RP phase

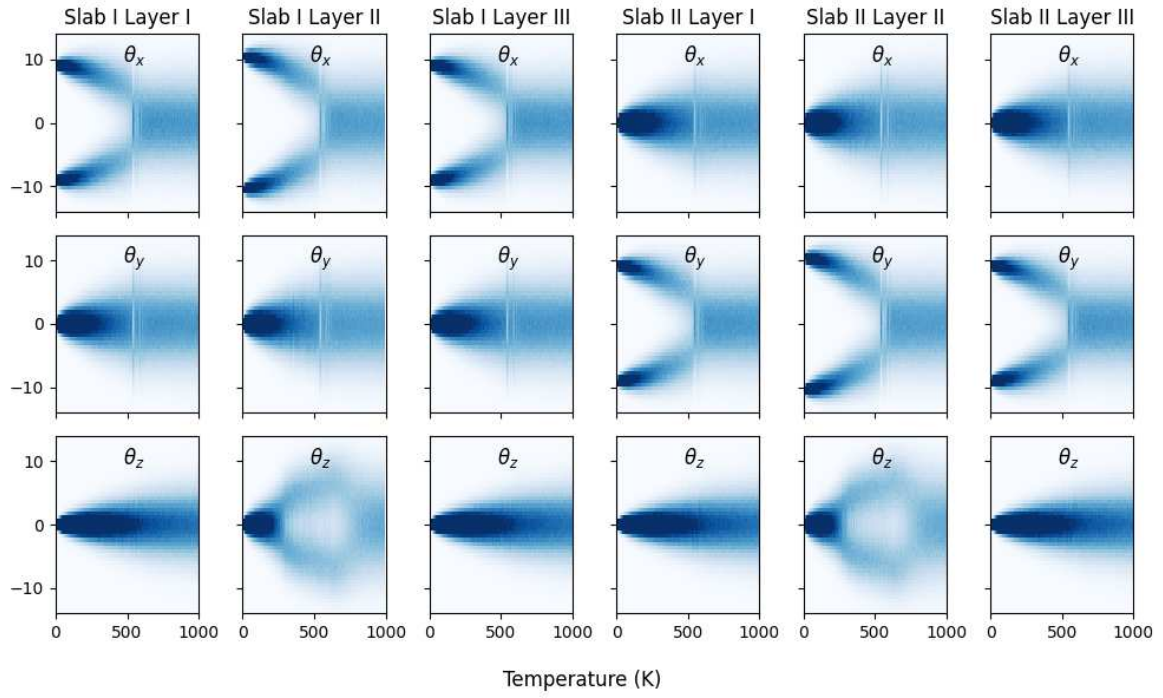


Figure S24: Euler angles of the $n = 3$ RP phase

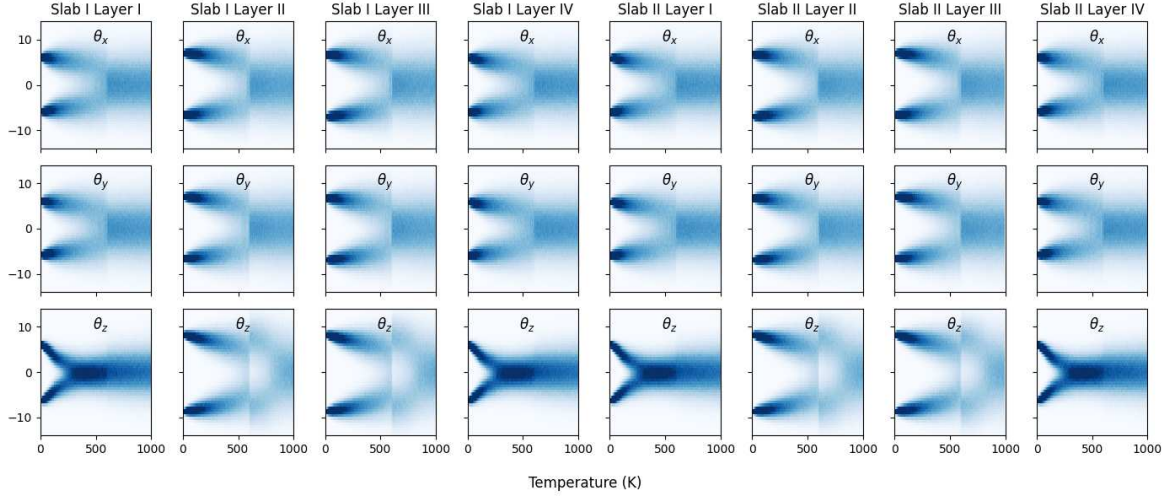


Figure S25: Euler angles of the $n = 4$ RP phase

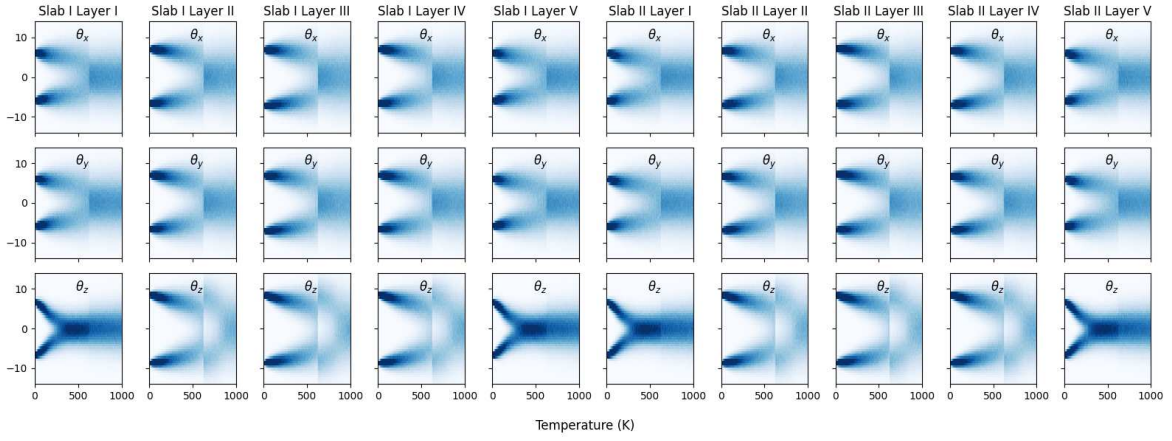


Figure S26: Euler angles of the $n = 5$ RP phase

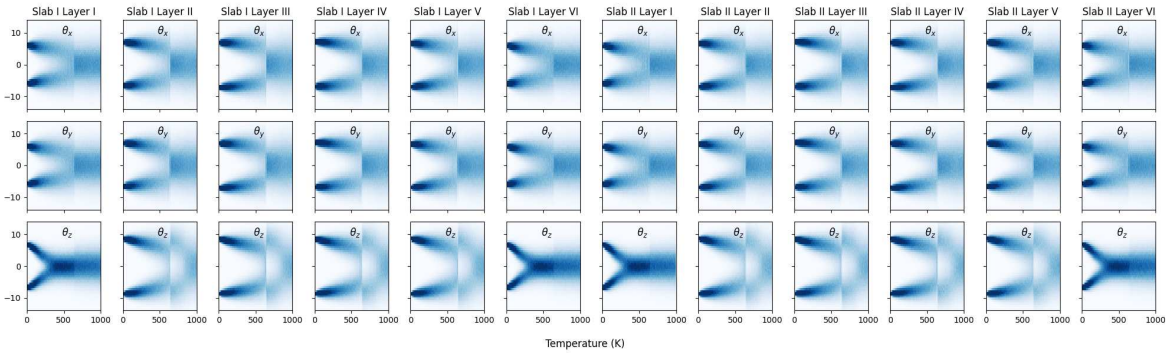


Figure S27: Euler angles of the $n = 6$ RP phase

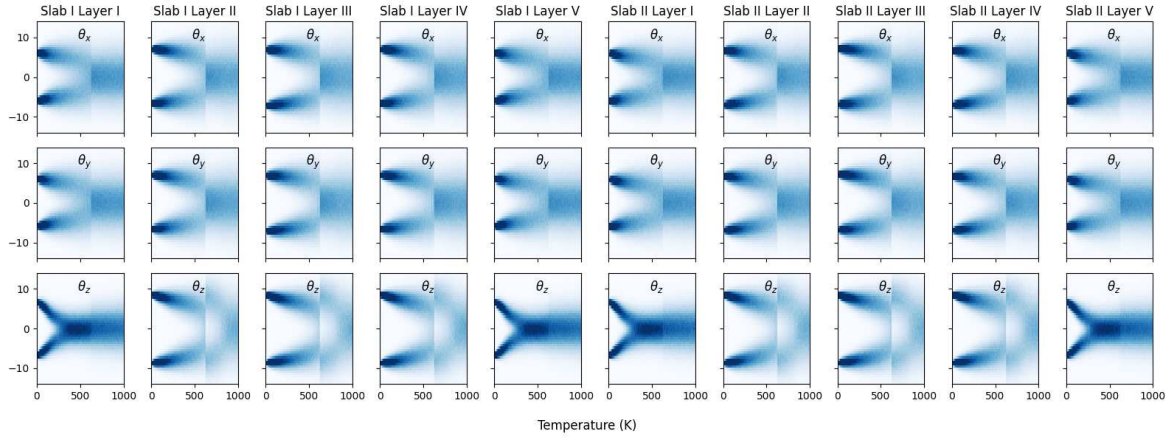


Figure S28: Euler angles of the $n = 5$ RP phase

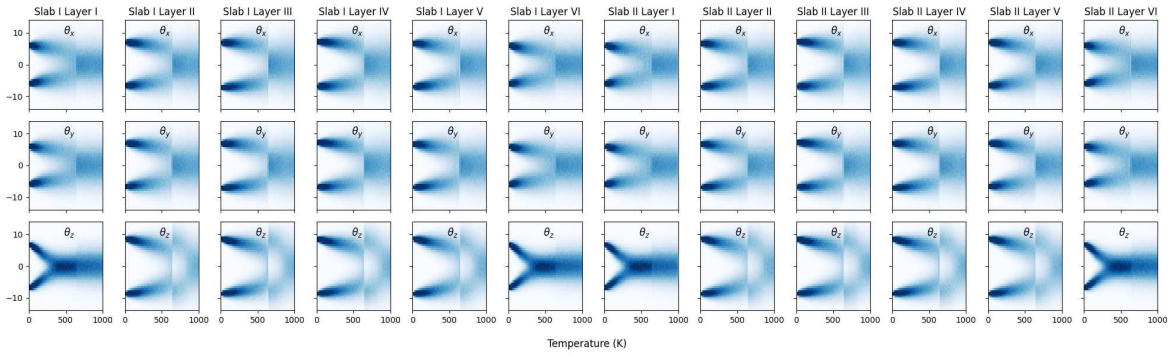


Figure S29: Euler angles of the $n = 6$ RP phase

Octahedral tilt angles for $n = 1$ to $n = 4$ RP phases

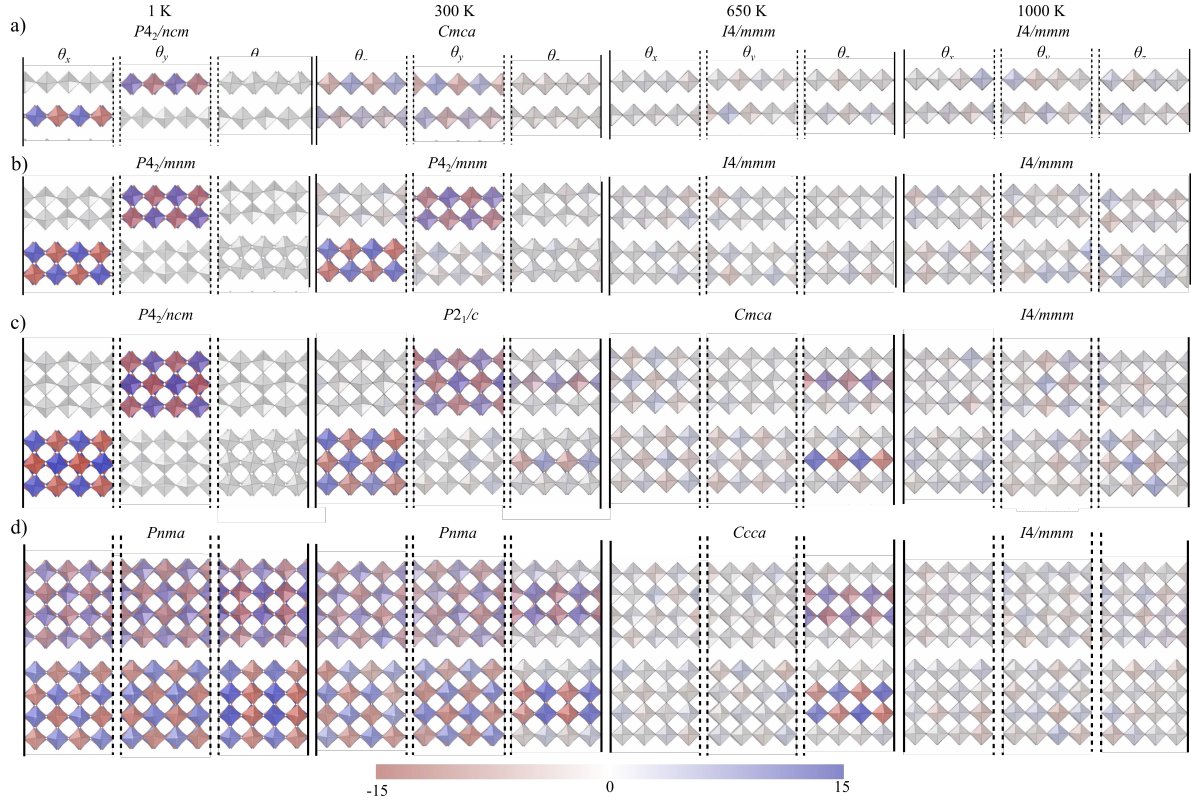


Figure S30: Snapshots of Euler angles (θ_x , θ_y , θ_z) of the ZrS_6 octahedra in the a) $n = 1$, b) $n = 2$, c) $n = 3$ and d) $n = 4$ RP polymorphs at four temperature points. The octahedra are colour-coded according to the magnitude of their tilt angles. Solid lines separate the structures by temperature, dashed lines separate the structures by tilt axis. The structures are viewed along the x-axis for θ_x and θ_z , and along the y-axis for θ_y .

Finite-temperature polymorphs

Space group and tilt pattern for each of the polymorphs observed in this study. The tilt patterns are given in Aleksandrov notation (see main text).

n	Space group	Aleksandrov
$n = 1$	$P4_2/ncm$	$\phi 00 \ 0\bar{\phi}0$
	$Cmca$	$\phi\phi 0 \ \bar{\phi}\bar{\phi}0$
	$I4/mmm$	$000 \ 000$
$n = 2$	$P4_2/mnm$	$\phi 00 \ 0\phi 0$
	$I4/mmm$	$000 \ 000$
$n = 3$	$P4_2/ncm$	$\phi 00 \ 0\bar{\phi}0$
	$P2_1/c$	$\phi 0\psi \ 0\phi\bar{\psi}$
	$Cmca$	$00\phi \ 00\phi$
	$I4/mmm$	$000 \ 000$
$n = 4$	$Pnma$	$\phi\phi\psi \ \phi\phi\bar{\psi}$
	$Ccce$	$00\phi \ 00\phi$
	$I4/mmm$	$000 \ 000$
$n = 5$	$P2_1/c$	$\phi\phi\psi \ \bar{\phi}\bar{\phi}\bar{\psi}$
	$Cmca$	$00\phi \ 00\phi$
	$I4/mmm$	$000 \ 000$
$n = 6$	$Pnma$	$\phi\phi\psi \ \phi\phi\bar{\psi}$
	$Ccce$	$00\phi \ 00\phi$
	$I4/mmm$	$000 \ 000$
$n = 7$	$P2_1/c$	$\phi\phi\psi \ \bar{\phi}\bar{\phi}\bar{\psi}$
	$Cmca$	$00\phi \ 00\phi$
	$I4/mmm$	$000 \ 000$
$n = 8$	$P2_1/c$	$\phi\phi\psi \ \phi\phi\bar{\psi}$
	$Cmca$	$00\phi \ 00\phi$
	$I4/mmm$	$000 \ 000$
$n = \infty$	$Pnma$	$\phi\phi\psi$
	$I4/mcm$	00ϕ
	$Pm\bar{3}m$	000

Table S3: Space group and tilt pattern for each of the polymorphs observed in this study.

A-site displacements

Rumpling refers to the displacement of A-site cations along the z -direction, predominantly occurring within the rocksalt layers. Here, we present the layer-resolved rumpling amplitudes for RP phases with $n = 1$ to 6. Our analysis reveals that rumpling is most pronounced at the outermost layers, at the rocksalt interfaces. The rumpling amplitudes are symmetric across the layers of the slab and remain the same between the two slabs in each RP phase.

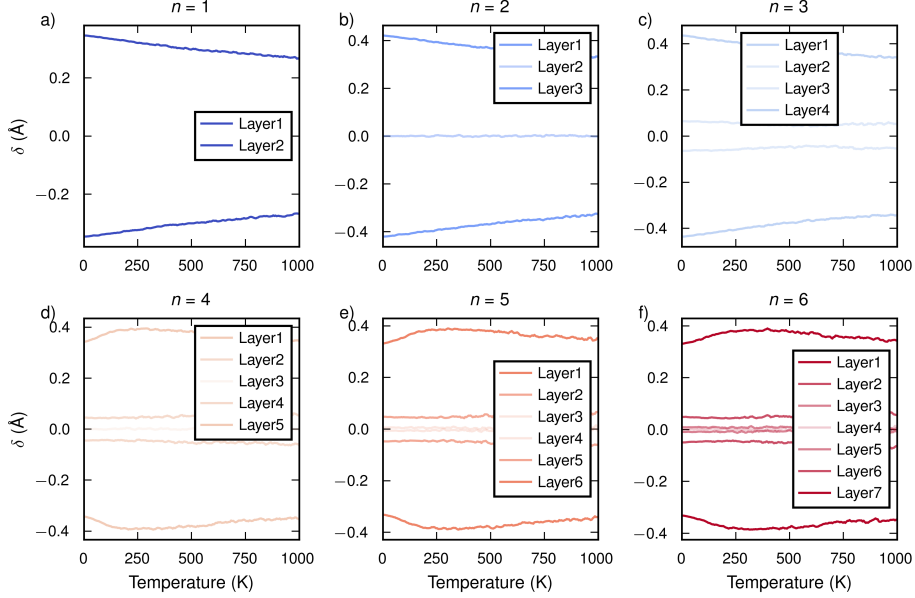


Figure S31: Layer-by-layer rumpling amplitude in the $n = 1$ to 6 RP phases

The competition between rumpling and tilting results from both distortions adjusting the in-plane Ba-S distances; out-of-plane octahedral tilting reduces the distance between Ba and S. This effect is demonstrated in Table S4, where the distance between Ba and S atoms in the rocksalt layer are provided for the untilted $I4/mmm$ structures and the ground-state tilted structure. In both cases a rumpling distortion has been applied.

n	$I4/mmm$	Ground state
1	3.56	3.26
2	3.58	3.24
3	3.59	3.24
4	3.59	3.21
5	3.59	3.21
6	3.89	3.21

Table S4: In-plane Ba-S distances in $Ba_{n+1}Zr_nS_{3n+1}$ for the untilted $I4/mmm$ structures and the ground-state tilted structure. Distances are given in Å. In both cases a rumpling distortion has been applied.

Next, we look at A-site displacements in the xy -plane. Here, the displacements are computed with the high-symmetry $I4/mmm$ structure as reference. For $n = 1, 2, 3$ the A-site displacements alternate within a layer (normal along z -axis) - see Fig. S32, Fig. S33, Fig. S34. Additionally, one can clearly see how the A-site displacements in the x and y directions follows that of the out of phase tilting around the x and y axes. For example, in $n = 1$ at 0K we have a tilting pattern of $\psi00\ 0\psi0$, and A-sites in the first slab are only displaced in the x -direction whereas in second slab they are displaced in the

y-direction. As the system transitions to $\psi\psi0 \ \psi\psi0$ we see both slabs exhibiting A-site displacements along both x and y direction. Finally, as the system transitions to untilted $I4/mmm$ phase the A-site displacements disappear.

However, in $n = 4$ (and above) the in-plane A-site displacements within one layer are all going in more or less the same direction. We note that within slab I there is thus a net displacement of A-sites, however this cancels out as the net displacements in slab II is in the opposite direction. This is expected for the $Pnma$ structure as it does not exhibit the improper ferroelectric behaviour seen in the $Cmc2_1$ structure.

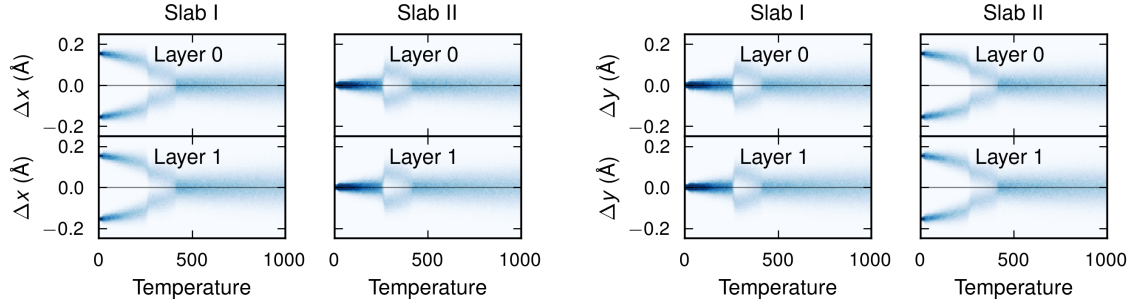


Figure S32: A-site displacements in the $n = 1$ RP phase

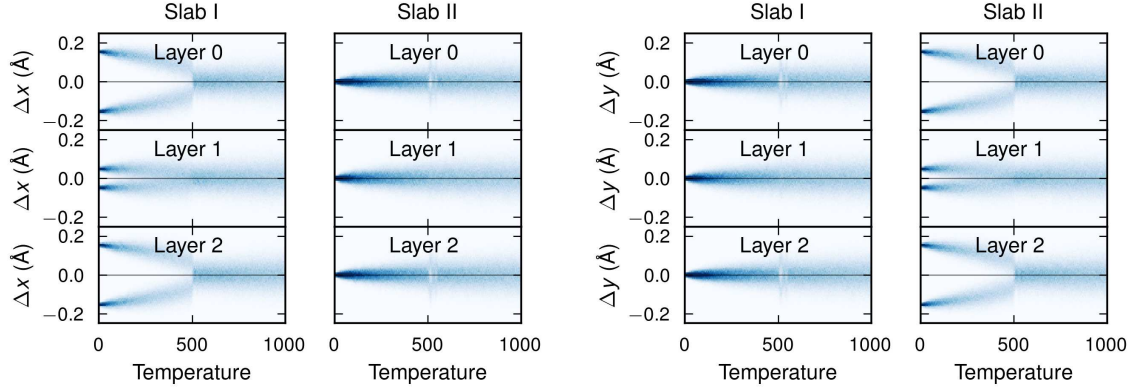


Figure S33: A-site displacements in the $n = 2$ RP phase

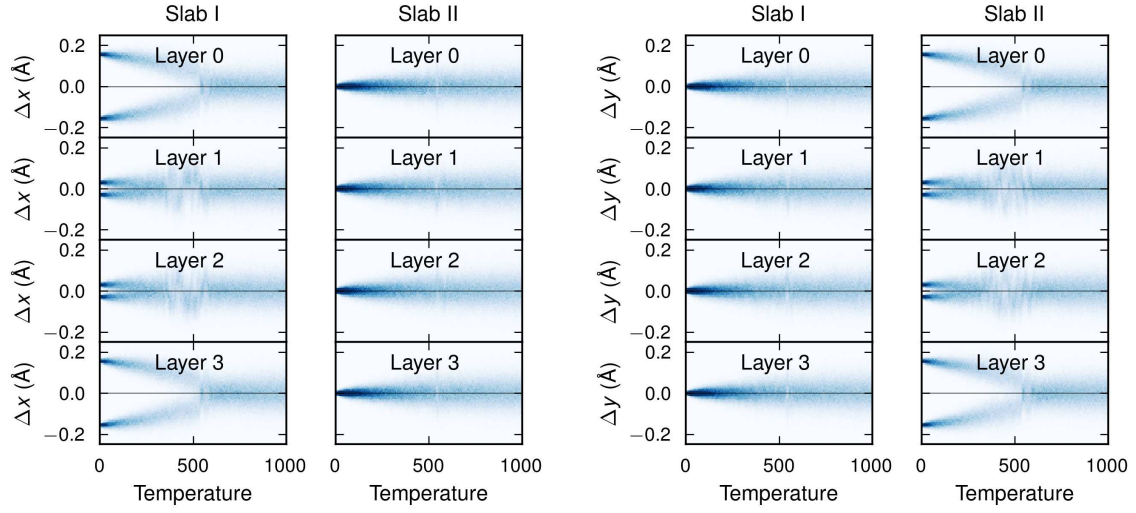


Figure S34: A-site displacements in the $n = 3$ RP phase

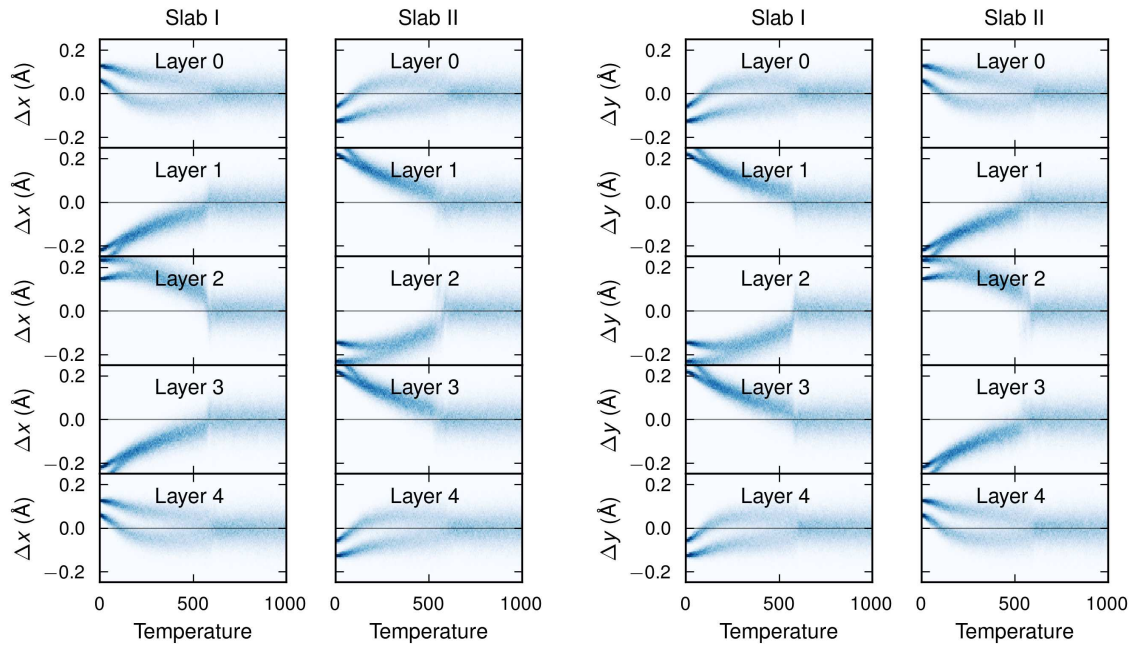


Figure S35: A-site displacements in the $n = 4$ RP phase

X-ray diffraction

X-ray diffraction (XRD) patterns were obtained by using the VESTA software using experimental values for the lattice parameters[?].

In Fig. S36, we show excellent agreement with the experimentally reported $P4_2/mnm$ phase at room temperature.

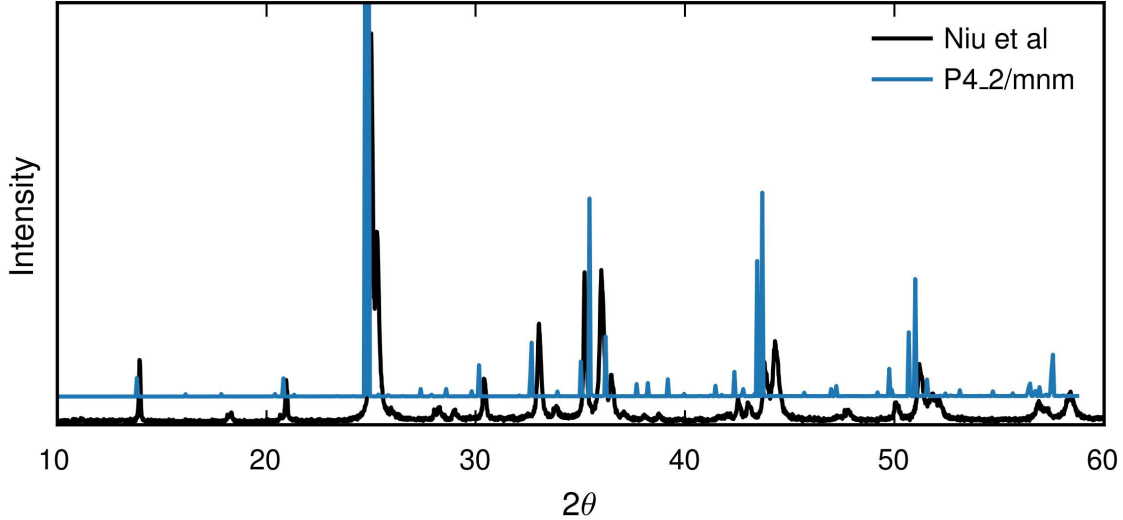


Figure S36: X-ray diffraction patterns for different phases of $\text{Ba}_3\text{Zr}_2\text{S}_7$. Experimental results are from Ref. 55.

In Fig. S37, we show the simulated XRD for three different phases of the $n = 1$ RP material – the low temperature $P4_2/nm$ polymorph, the intermediate $Cmca$, and the high temperature $I4/mmm$ polymorph. We also plot the experimentally reported data from Ref. 55 for comparison (where it is assigned to $I4/mmm$).

We find that, as expected for such closely-related structures, the XRD patterns of all phases are highly similar. At room temperature our heating simulations predict the $Cmca$ phase to be stable. This assignment is supported by peak shoulders at 25° and 36° in the experimental XRD. However, there are also a number of peaks missing in the experimental XRD at 18° , 32° , and 50° . XRD patterns can have broad and unresolved peaks for polycrystalline samples of BaZrS_3 [?]. In addition, we note that the peaks associated with the $Cmca$ will gradually decrease in intensity with increasing temperature due to its predicted second-order transition to the $I4/mmm$ phase at 400 K. The phase transition temperatures are sensitive to the small energy differences between polymorphs, and so although we can tentatively assign the experimental XRD pattern to the $Cmca$ phase, we cannot rule out formation of the $P4_2/nm$ or $I4/mmm$ phases at room temperature. Further XRD measurements on a single crystal sample, combined with complementary techniques such as Raman spectroscopy could aid in a more definite determination of the crystal structure.

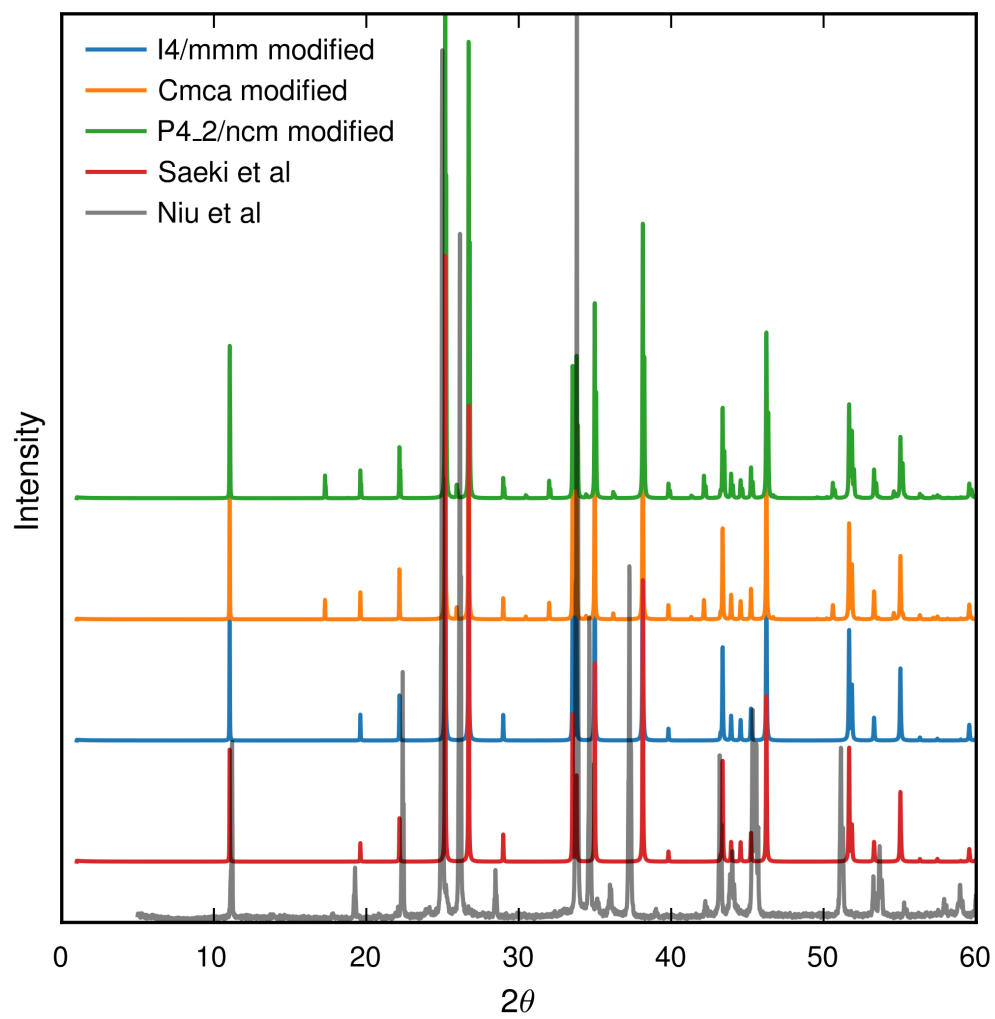


Figure S37: X-ray diffraction patterns for different phases of Ba_2ZrS_4 . Experimental results are from Ref. 29 and Ref. 2.

Supplemental References

- [1] M. S. B. Hoque, E. R. Hoglund, B. Zhao, D.-L. Bao, H. Zhou, S. Thakur, E. Osei-Agyemang, K. Hattar, E. A. Scott, M. Surendran, J. A. Tomko, J. T. Gaskins, K. Aryana, S. Makarem, A. Alwen, A. M. Hodge, G. Balasubramanian, A. Giri, T. Feng, J. A. Hachtel, J. Ravichandran, S. T. Pantelides, and P. E. Hopkins, *Nature Communications* **16**, 6104 (2025).
- [2] S. Niu, D. Sarkar, K. Williams, Y. Zhou, Y. Li, E. Bianco, H. Huyan, S. B. Cronin, M. E. McConney, R. Haiges, *et al.*, *Chemistry of Materials* **30**, 4882 (2018).
- [3] C. Ming, K. Yang, H. Zeng, S. Zhang, and Y.-Y. Sun, *Material Horizons* **7**, 2985 (2020).
- [4] M. A. Yattoo and S. J. Skinner, *Materials Today: Proceedings* **56**, 3747 (2022).
- [5] J. Kim, J. Mun, C. M. Palomares Garcíá, B. Kim, R. S. Perry, Y. Jo, H. Im, H. G. Lee, E. K. Ko, S. H. Chang, *et al.*, *Nano Letters* **21**, 4185 (2021).
- [6] M. Zhang, C. Pei, Q. Wang, Y. Zhao, C. Li, W. Cao, S. Zhu, J. Wu, and Y. Qi, *Journal of Materials Science & Technology* **185**, 147 (2024).
- [7] M. Markov, L. Alaerts, H. P. C. Miranda, G. Petretto, W. Chen, J. George, E. Bousquet, P. Ghosez, G.-M. Rignanese, and G. Hautier, *Proceedings of the National Academy of Sciences* **118**, e2026020118 (2021).
- [8] G. Clarke, D. Daisenberger, X. Luo, S. Cheong, N. C. Bristowe, and M. S. Senn, *Physical Review B* **109**, 094107 (2024).
- [9] N. Z. Koocher, L.-F. Huang, and J. M. Rondinelli, *Physical Review Materials* **5**, 053601 (2021).
- [10] M. S. Senn, C. A. Murray, X. Luo, L. Wang, F.-T. Huang, S.-W. Cheong, A. Bombardi, C. Ablitt, A. A. Mostofi, and N. C. Bristowe, *Journal of the American Chemical Society* **138**, 5479 (2016), <https://doi.org/10.1021/jacs.5b13192>.
- [11] Y.-Y. Sun, M. L. Agiorgousis, P. Zhang, and S. Zhang, *Nano Letters* **15**, 581 (2015).
- [12] K. V. Sopiha, C. Comparotto, J. A. Márquez, and J. J. Scragg, *Adv. Opt. Mater.* **10**, 2101704 (2022).
- [13] D. Tiwari, O. S. Hutter, and G. Longo, *J. Phys.: Energy* **3**, 034010 (2021).
- [14] R. Jaramillo and J. Ravichandran, *APL Mater.* **7**, 100902 (2019).
- [15] J. W. Choi, B. Shin, P. Gorai, R. L. Hoye, and R. Palgrave, *Emerging earth-abundant solar absorbers* (2022).
- [16] X. Song, X. Shai, S. Deng, J. Wang, J. Li, X. Ma, X. Li, T. Wei, W. Ren, L. Gao, Y. Fu, H. Wang, and C. Zeng, *The Journal of Physical Chemistry C* **126**, 11751 (2022), <https://doi.org/10.1021/acs.jpcc.2c02286>.
- [17] Z. Yang, Y. Han, Y. Liang, W. Shen, Z. Zhang, C. Fang, Q. Wang, B. Wan, L. Chen, Y. Zhang, *et al.*, *Acta Materialia*, 120156 (2024).
- [18] E. Osei-Agyemang and G. Balasubramanian, *ACS Applied Energy Materials* **3**, 1139 (2019).
- [19] E. Osei-Agyemang, N. Koratkar, and G. Balasubramanian, *Journal of Materials Chemistry C* **9**, 3892 (2021).
- [20] Y. Wu, Y. Chen, Z. Fang, Y. Ding, Q. Li, K. Xue, H. Shao, H. Zhang, and L. Zhou, *The Journal of Physical Chemistry Letters* **14**, 11465 (2023).
- [21] Y. Zhang, T. Shimada, T. Kitamura, and J. Wang, *The journal of physical chemistry letters* **8**, 5834 (2017).

- [22] H. Wang, G. Gou, and J. Li, *Nano Energy* **22**, 507 (2016).
- [23] X. Wu, W. Gao, J. Chai, C. Ming, M. Chen, H. Zeng, P. Zhang, S. Zhang, and Y.-Y. Sun, *Science China Materials* **64**, 2976 (2021).
- [24] Z. Yuan, D. Dahliah, R. Claes, A. Pike, D. P. Fenning, G.-M. Rignanese, and G. Hautier, *PRX Energy* **3**, 033008 (2024).
- [25] Y. Jiang, H. K. D. Le, L. Verbitsky, H. DeVyldere, A. M. Oddo, B. Pan, H.-g. Song, C. Zhu, H. Zhu, M. C. Scott, and P. Yang, *Nano Letters* **25**, 7029 (2025), pMID: 40249145, <https://doi.org/10.1021/acs.nanolett.5c00815>.
- [26] R. S. Nielsen, Ángel Labordet Álvarez, Y. Tømm, G. Gurieva, A. Ortega-Guerrero, J. Breternitz, L. Bastonero, N. Marzari, C. A. Pignedoli, S. Schorr, and M. Dimitrievska, *BaZrS₃ Lights Up: The Interplay of Electrons, Photons, and Phonons in Strongly Luminescent Single Crystals* (2025), arXiv:2503.16180 [cond-mat.mtrl-sci].
- [27] Y. Nishigaki, T. Nagai, M. Nishiwaki, T. Aizawa, M. Kozawa, K. Hanzawa, Y. Kato, H. Sai, H. Hiramatsu, H. Hosono, *et al.*, *Solar Rrl* **4**, 1900555 (2020).
- [28] Y.-C. Hung, J. Fetting, and B. Eichhorn, *Crystal Structure Communications* **53**, 827 (1997).
- [29] M. Saeki, Y. Yajima, and M. Onoda, *Journal of Solid State Chemistry* **92**, 286 (1991).
- [30] B.-H. Chen, B. Eichhorn, and W. Wong-Ng, *Crystal Structure Communications* **50**, 161 (1994).
- [31] S. Niu, J. Milam-Guerrero, Y. Zhou, K. Ye, B. Zhao, B. C. Melot, and J. Ravichandran, *Journal of Materials Research* **33**, 4135 (2018).
- [32] B.-H. Chen, W. Wong-Ng, and B. W. Eichhorn, *Journal of Solid State Chemistry* **103**, 75 (1993).
- [33] P. Kayastha, E. Fransson, P. Erhart, and L. Whalley, *The Journal of Physical Chemistry Letters* **16**, 2064 (2025).
- [34] K. Aleksandrov, *Crystallography Reports* **40** (1995).
- [35] Z. Fan, Z. Zeng, C. Zhang, Y. Wang, K. Song, H. Dong, Y. Chen, and T. Ala-Nissila, *Physical Review B* **104**, 104309 (2021).
- [36] Z. Fan, *Journal of Physics: Condensed Matter* **34**, 125902 (2022).
- [37] Z. Fan, Y. Wang, P. Ying, K. Song, J. Wang, Y. Wang, Z. Zeng, K. Xu, E. Lindgren, J. M. Rahm, A. J. Gabourie, J. Liu, H. Dong, J. Wu, Y. Chen, Z. Zhong, J. Sun, P. Erhart, Y. Su, and T. Ala-Nissila, *The Journal of Chemical Physics* **157**, 114801 (2022).
- [38] J. Heyd, G. E. Scuseria, and M. Ernzerhof, *The Journal of Chemical Physics* **118**, 8207 (2003).
- [39] V. Blum, R. Gehrke, F. Hanke, P. Havu, V. Havu, X. Ren, K. Reuter, and M. Scheffler, *Computer Physics Communications* **180**, 2175 (2009).
- [40] F. Knoop, T. Purcell, M. Scheffler, and C. Carbogno, *The Journal of Open Source Software* **5** (2020).
- [41] See supplemental material at [url will be inserted by publisher] for further calculation details and analysis (2025).
- [42] A. H. Larsen, J. J. Mortensen, J. Blomqvist, I. E. Castelli, R. Christensen, M. Dułak, J. Friis, M. N. Groves, B. Hammer, C. Hargus, E. D. Hermes, P. C. Jennings, P. B. Jensen, J. Kermode, J. R. Kitchin, E. L. Kolsbjerg, J. Kubal, K. Kaasbjerg, S. Lysgaard, J. B. Maronsson, T. Maxson, T. Olsen, L. Pastewka, A. Peterson, C. Rostgaard, J. Schiøtz, O. Schütt, M. Strange, K. S. Thygesen, T. Vegge, L. Vilhelmsen, M. Walter, Z. Zeng, and K. W. Jacobsen, *Journal of Physics: Condensed Matter* **29**, 273002 (2017).

- [43] E. Lindgren, M. Rahm, E. Fransson, F. Eriksson, N. Österbacka, Z. Fan, and P. Erhart, *Journal of Open Source Software* **9**, 6264 (2024).
- [44] J. P. Perdew, A. Ruzsinszky, G. I. Csonka, O. A. Vydrov, G. E. Scuseria, L. A. Constantin, X. Zhou, and K. Burke, *Physical Review Letters* **100**, 136406 (2008).
- [45] A. Togo, *Journal of the Physical Society of Japan* **92**, 012001 (2023).
- [46] A. Togo, K. Shinohara, and I. T. and, *Science and Technology of Advanced Materials: Methods* **4**, 2384822 (2024).
- [47] A. Stukowski, *Modelling and Simulation in Materials Science and Engineering* **18**, 015012 (2009).
- [48] F. Eriksson, E. Fransson, and P. Erhart, *Advanced Theory and Simulations* **2**, 1800184 (2019).
- [49] E. Fransson, J. Wiktor, and P. Erhart, *The Journal of Physical Chemistry C* **127**, 13773 (2023).
- [50] E. Fransson, J. Wiktor, and P. Erhart, *ACS Energy Letters* **9**, 3947 (2024).
- [51] E. Fransson, P. Rosander, F. Eriksson, J. M. Rahm, T. Tadano, and P. Erhart, *Communications Physics* **6**, 173 (2023).
- [52] K. S. Aleksandrov, B. V. Beznosikov, and S. V. Misyul, *Physica Status Solidi (a)* **104**, 529 (1987).
- [53] C. Ablitt, S. Craddock, M. S. Senn, A. A. Mostofi, and N. C. Bristowe, *npj Computational Materials* **3**, 10.1038/s41524-017-0040-0 (2017).
- [54] N. Z. Koocher, A. B. Altman, R. A. Klein, C. D. Malliakas, S. D. Jacobsen, D. E. Freedman, and J. M. Rondinelli, *Inorganic Chemistry* **64**, 10761 (2025), pMID: 40413650, <https://doi.org/10.1021/acs.inorgchem.5c00314> .
- [55] S. Niu, B. Zhao, K. Ye, E. Bianco, J. Zhou, M. E. McConney, C. Settens, R. Haiges, R. Jaramillo, and J. Ravichandran, *Journal of Materials Research* **34**, 3819 (2019).
- [56] Perez-Mato, J.M., Aroyo, M.I., and Orobengoa, D., *EPJ Web of Conferences* **22**, 00008 (2012).
- [57] M. H. Christensen, P. P. Orth, B. M. Andersen, and R. M. Fernandes, *Phys. Rev. Lett.* **121**, 057001 (2018).
- [58] Y. Zhang, J. Wang, and P. Ghosez, *Phys. Rev. Lett.* **125**, 157601 (2020).
- [59] T. Birol, N. A. Benedek, and C. J. Fennie, *Physical Review Letters* **107**, 257602 (2011).
- [60] G. Stone, C. Ophus, T. Birol, J. Ciston, C.-H. Lee, K. Wang, C. J. Fennie, D. G. Schlom, N. Alem, and V. Gopalan, *Nature Communications* **7**, 12572 (2016).